

# Measurement of the Hubble Constant from X-ray and 2.1 mm Observations of Abell 2163.

W. L. Holzapfel<sup>1</sup>, M. Arnaud<sup>2</sup>, P. A. R. Ade<sup>3</sup>, S. E. Church<sup>4</sup>,  
M. L. Fischer<sup>5</sup>, P. D. Mauskopf<sup>4,6</sup>, Y. Rephaeli<sup>7</sup>, T. M. Wilbanks<sup>8</sup> and A. E. Lange<sup>4</sup>

## ABSTRACT

We report 2.1 mm observations of the Sunyaev-Zel'dovich (S-Z) effect; these observations confirm our previous detection of a decrement in the Cosmic Microwave Background intensity towards the cluster Abell 2163. The S-Z data are analyzed using the relativistically correct expression for the Comptonization. We begin by assuming the intracluster (IC) gas to be isothermal at the emission weighted average temperature determined by a combined analysis of the ASCA and GINGA X-ray satellite observations. The results of ROSAT/PSPC observations are used to determine an isothermal model for the S-Z surface brightness. Fitting to this model, we determine the peak Comptonization to be  $y_0 = 3.73_{-0.61}^{+0.47} \times 10^{-4}$ . The uncertainty includes contributions due to statistical uncertainty in the detection, instrumental baseline, calibration, and density model. Combining the X-ray and S-Z measurements, we determine the Hubble constant to be  $H_0(q_0 = \frac{1}{2}) = 60_{-23}^{+40} \text{ kms}^{-1} \text{ Mpc}^{-1}$ , where the uncertainty is dominated by the systematic difference in the ASCA and GINGA determined IC gas temperatures. ASCA observations suggest the presence of a significant thermal gradient in the IC gas. We determine  $H_0$  as a function of the assumed IC gas thermal structure. Using the ASCA determined thermal structure and keeping the emission weighted average temperature the same as in the isothermal case, we find  $H_0(q_0 = \frac{1}{2}) = 78_{-28}^{+54} \text{ kms}^{-1} \text{ Mpc}^{-1}$ . Including additional uncertainties due to cluster asphericity, peculiar velocity, IC gas clumping, and astrophysical confusion, we find  $H_0(q_0 = \frac{1}{2}) = 78_{-40}^{+60} \text{ kms}^{-1} \text{ Mpc}^{-1}$ .

*Subject headings:* cosmology: observations — distance scale — cosmic microwave background — galaxies: clusters: individual (Abell 2163) — X-rays: galaxies

---

<sup>1</sup>Enrico Fermi Institute, University of Chicago, Chicago IL 60637

<sup>2</sup>C. E. A., DSM, DAPNIA, Service d'Astrophysique, CE Saclay, F-91191 Gif sur Yvette Cedex, France

<sup>3</sup>Department of Physics, Queen Mary and Westfield College, Mile End Road, London, E1 4NS, U.K.

<sup>4</sup>Department of Physics, Math, and Astronomy, California Institute of Technology, Pasadena CA 91125

<sup>5</sup>Energy & Environment Division, Lawrence Berkeley Laboratory, Berkeley, CA 94720

<sup>6</sup>Department of Physics, University of California, Berkeley, CA 94720

<sup>7</sup>Center for Particle Astrophysics, University of California, Berkeley, CA 94720

<sup>8</sup>Aradigm Corporation, Hayward CA 94545

## 1. Introduction

Compton scattering of the cosmic microwave background (CMB) radiation by hot intracluster (IC) gas – the Sunyaev-Zel’dovich (S-Z) effect – gives rise to an observable distortion of the CMB spectrum which can be used as a sensitive cosmological probe. The intensity change caused by the scattering has a thermal component, due to the random motions of the scattering electrons (Sunyaev & Zel’dovich 1972), and a kinematic component, due to the bulk peculiar velocity of the IC gas (Sunyaev & Zel’dovich 1980). When combined with X-ray measurements, the amplitude of the thermal component can be used to determine the Hubble constant (Gunn 1978; Cavaliere *et al.* 1979). The ratio of the amplitudes of thermal and kinematic components can be combined with the X-ray temperature to determine the radial component of the cluster peculiar velocity (Sunyaev & Zel’dovich 1980; Rephaeli & Lahav 1991). Because the surface brightness of the S-Z effect is independent of redshift, this method for determining the Hubble constant and cluster peculiar velocities can be applied to distant clusters, provided the requisite X-ray data can be obtained.

The thermal and kinematic components of the S-Z effect have distinct spectral shapes and can be separated from one another by measurements at two or more millimeter (mm) wavelengths. Astrophysical confusion for the S-Z effect exhibits a broad minimum at wavelengths of 2 – 3 mm (Fischer & Lange 1993). Several significant detections of the S-Z effect at centimeter (cm) wavelengths have been reported in recent years. Some of these measurements have been combined with X-ray observations to compute values for  $H_0$  (Birkinshaw, Hughes & Arnaud 1991; Birkinshaw & Hughes 1994; Herbig *et al.* 1995; Jones *et al.* 1993; Myers *et al.* 1995; for a recent review, see Rephaeli 1995a). The prospect of separating the thermal and kinematic components of the S-Z effect while minimizing astrophysical confusion makes observations at mm wavelengths attractive.

We have developed a novel instrument and observing strategy with high sensitivity to the S-Z effect in several millimeter bands (Holzapfel *et al.* 1996a). Using this instrument, we have detected the S-Z effect in the direction of the cluster Abell 2163 (Wilbanks *et al.* 1994 – hereafter W94). A2163 is a rich, moderately distant ( $z = .201$ , Soucail *et al.* 1995) cluster of galaxies, which has been observed in the X-ray with

the Einstein, GINGA, ROSAT, and ASCA satellites (Arnaud *et al.* 1992; Elbaz *et al.* 1995; Markevitch *et al.* 1996). Its X-ray luminosity and temperature are among the highest of any cluster yet studied, implying a high IC gas density and temperature, and correspondingly high S-Z surface brightness. The low declination and modest angular extent of this cluster make it a good candidate for observations with our instrument, which operates by drift scanning (see Sections 4.1. & 4.2.). In this paper, we combine observations of the S-Z effect and X-ray emission to determine  $H_0$ . This is the first determination of  $H_0$  from millimeter wavelength measurements of the S-Z effect.

The determination of  $H_0$  presented here includes several refinements with respect to previous work.

1.) We use a relativistically correct calculation of CMB Comptonization in clusters. The nonrelativistic treatment is inaccurate at high frequencies and high IC gas temperatures (see Section 2.1.). Use of the relativistically correct formulae in the analysis of 2.1 mm measurements of A2163, the hottest known X-ray cluster, is essential in order to derive an accurate value of  $H_0$ .

2.) We use the combination of the ROSAT derived density profile and the S-Z surface brightness to constrain models for the large scale thermal structure of the IC gas. The allowed range of thermal structure models is compared to that determined from the combination of ASCA and ROSAT measurements. We have determined  $y_0$  and  $H_0$  as a function of the cluster thermal structure, specifically for the thermal structure measured by ASCA.

3.) Finally, we include a detailed analysis of additional contributions to the uncertainty in  $H_0$  due to uncertainties in the distribution and thermal structure of the IC gas, the possibility that the cluster has an appreciable peculiar velocity, and astrophysical confusion to the S-Z effect.

In Section 2., we briefly review the relativistic Comptonization calculation and outline the method used to determine  $H_0$  from S-Z and X-ray measurements. The analysis of the X-ray data is outlined in Section 3.. The SuZIE instrument, its calibration, and observations of A2163 are described in 4.. In Section 5., we describe the analysis of the S-Z data under the assumption of isothermal gas. We combine the isothermal S-Z and X-ray results to determine the Hubble constant in Section 6.. In Section 7., we dis-

cuss the large scale thermal structure of the IC gas and its effects on our results. Additional contributions to the uncertainty in  $H_0$  are discussed in Section 8.; our conclusions are summarized in Section 9..

## 2. Theory

### 2.1. Relativistic Comptonization in Clusters

The Sunyaev & Zel'dovich (1972) treatment of CMB Comptonization by hot IC gas is based on a solution to the Kompaneets (1957) equation, a non-relativistic diffusion approximation to the full kinematic equation for the change of the photon distribution. The expression derived for the intensity change – an expression which has been used in virtually all works on the S-Z effect in clusters – is valid only at low gas temperatures. A more accurate calculation of the thermal effect requires use of the relativistic form for the electron velocity distribution and the full expression for the scattering probability, as has been presented by Rephaeli (1995b). Use of the correct relativistic calculation in this work is essential because of the high observing frequency and the unusually high IC gas temperature in A2163.

In the nonrelativistic limit, the CMB intensity change due to Compton scattering by a hot electron gas (with no bulk velocity) is (Zel'dovich & Sunyaev 1968)

$$\Delta I_{nr} = I_0 y g(x), \quad (1)$$

where  $x = h\nu/kT_0$ ,  $T_0$  is the CMB temperature, and

$$I_0 \equiv \frac{2(kT_0)^3}{(hc)^2}. \quad (2)$$

The spectrum is given by the function,

$$g(x) = \frac{x^4 e^x}{(e^x - 1)^2} \left[ \frac{x(e^x + 1)}{e^x - 1} - 4 \right], \quad (3)$$

which vanishes at  $x_0 = 3.83$  ( $\nu_0 = 217$  GHz) for  $T_0 = 2.726$  K (Mather *et al.* 1994). The Comptonization parameter is given by,

$$y = \int \left( \frac{kT_e}{mc^2} \right) n_e \sigma_T dl, \quad (4)$$

where  $n_e$  and  $T_e$  are the electron density and temperature,  $\sigma_T$  is the Thomson cross section, and the integral is over a line of sight through the cluster.

As has been shown by Wright (1979), the exact scattered photon distribution can be calculated using

the Chandrasekhar (1950) expression for the scattering probability and the relativistically correct form for the Maxwellian electron velocity distribution. Integrations over the scattering angle, electron velocities, and incident (Planck) spectrum, yield an expression for the intensity change (Rephaeli 1995b),

$$\Delta I = I_0 \int \Psi(x, T_e) d\tau, \quad (5)$$

where  $d\tau = n_e \sigma_T dl$ . The spectrum is given by

$$\Psi(x, T_e) = \frac{x^3}{(e^x - 1)} [\Phi(x, T_e) - 1], \quad (6)$$

where  $\Phi(x, T_e)$  is a three dimensional integral over electron scattering angles, velocities, and the change in frequency of the scattered photons which is fully specified in Rephaeli (1995b). This calculation is exact to first order in  $\tau$ . In Fig. 1, we compare the relativistic and nonrelativistic expressions, at the GINGA + ROSAT derived isothermal gas temperature in A2163,  $kT_e = 14.6$  keV (Elbaz *et al.* 1995).

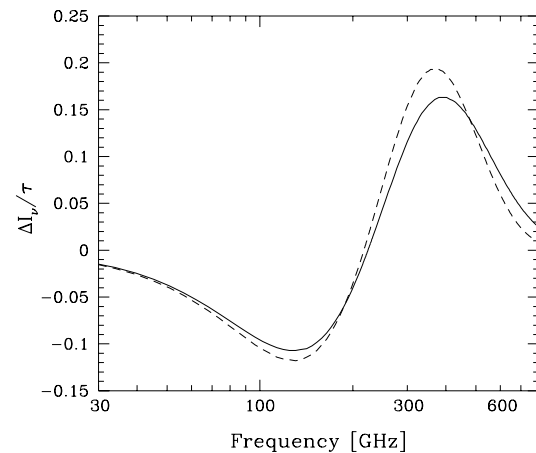


Fig. 1.— The spectral forms of the intensity change due to the thermal Sunyaev-Zel'dovich effect and the non-relativistic approximation. The solid line shows  $\Delta I/\tau$ , and the dotted line shows  $\Delta I_{nr}/\tau$  (both in units of  $2(kT_0)^3/(hc)^2$ ) for  $kT_e = 14.6$  keV.

At the central frequency of the SuZIE 2.1 mm band ( $\nu \simeq 142$  GHz), the ratio of the brightnesses

is  $\Delta I/\Delta I_{nr} = .91$ . Finally, in order to facilitate comparison of our results with low frequency observations, we combine equations 4 and 5 to express an effective Comptonization in terms of the measured intensity change,

$$y = \frac{\Delta I}{I_0} \frac{\int \frac{kT_e}{m_e c^2} d\tau}{\int \Psi(x, T_e) d\tau}. \quad (7)$$

All results for the Comptonization presented in this paper are computed using this expression.

## 2.2. Hubble Constant from S-Z and X-Ray Measurements

The determination of  $H_0$  from the combination of X-ray and S-Z data has been treated by Birkinshaw, Hughes, & Arnaud (1991) – hereafter BHA. Their treatment is adopted here with some exceptions; we express the S-Z decrement in intensity rather than in Rayleigh-Jeans temperature and use a relativistically correct expression for the Comptonization.

Hot IC gas is detected primarily through its thermal bremsstrahlung X-ray emission. The X-ray surface brightness at energy  $E$  can be expressed as the line of sight integral (BHA equation 3.1),

$$b_X = \frac{1}{4\pi(1+z)^3} \int n_e^2 \Lambda(E, T_e) dl, \quad (8)$$

where  $n_e$  is the electron density,  $\Lambda(E, T_e)$  is the specific spectral emissivity, and  $z$  is the cluster redshift. We express the electron temperature, density, and spectral emissivity in terms of the product of a reference value and a dimensionless form factor (BHA equations 3.3 - 3.5):

$$n_e(r) = n_{e0} f_n(\theta, \phi, \xi), \quad (9)$$

$$T_e(r) = T_{e0} f_T(\theta, \phi, \xi), \quad (10)$$

$$\Lambda_e(E, T_e) = \Lambda_{e0} f_\Lambda(E, T_e), \quad (11)$$

where  $\theta$  is the angle from a reference line of sight,  $\phi$  is the azimuthal angle about that line of sight,  $\xi$  is the angular distance along the line of sight, and  $n_{e0}$  and  $T_{e0}$  are the central gas density and temperature. We extend this treatment to include a term describing the temperature dependence of relativistic Comptonization,

$$\Psi(x, T_e) = \Psi_0 f_\Psi(x, T_e). \quad (12)$$

The expressions for the X-ray and S-Z surface brightnesses, equations 8 and 5, then become:

$$b_X(\theta, \phi) = \frac{n_{e0}^2 \Lambda_{e0} d_A}{4\pi(1+z)^3} \int d\xi f_n^2 f_\Lambda, \quad (13)$$

$$\equiv N_X \Theta_X, \quad (14)$$

$$\Delta I(\theta, \phi) = I_0 \Psi_0 n_{e0} \sigma_T d_A \int d\xi f_n f_\Psi, \quad (15)$$

$$\equiv N_{SZ} \Theta_{SZ}, \quad (16)$$

where  $d_A$  is the angular diameter distance. The structural information for the cluster is contained in the angles:

$$\Theta_X = \int d\xi f_n^2 f_\Lambda, \quad (17)$$

$$\Theta_{SZ} = \int d\xi f_n f_\Psi. \quad (18)$$

The normalization factors are then defined as:

$$N_X = \frac{n_{e0}^2 \Lambda_{e0} d_A}{4\pi(1+z)^3}, \quad (19)$$

$$N_{SZ} = I_0 \Psi_0 n_{e0} \sigma_T d_A. \quad (20)$$

Eliminating the unknown central electron density between these equations, we can express  $d_A$  in terms of measurable quantities,

$$d_A = \left( \frac{N_{SZ}^2}{N_X} \right) \frac{\Lambda_{e0}}{4\pi(1+z)^3 [I_0 \Psi_0 \sigma_T]^2}, \quad (21)$$

which is an implicitly expressed generalization of BHA's equation (3.12) valid at all frequencies and gas temperatures. Combining  $N_X$  and  $N_{SZ}$  with a measurement of  $T_{e0}$ , which appears in the expressions for  $\Lambda_{e0}$  and  $\Psi_0$ , we can then solve for  $H_0(q_0) \propto 1/d_A$ .

Because we have no information about the distribution of the IC gas along the line of sight, we are required to make some simplifying assumptions about the temperature and density form factors. We assume that the density form factor can be described by a convenient empirical model (Cavaliere *et al.* 1976),

$$f_n(\theta) = \left( 1 + \frac{\theta^2}{\theta_c^2} \right)^{-\frac{3}{2}\beta}, \quad (22)$$

in which  $\beta$  and the cluster angular core radius ( $\theta_c$ ) are left as free parameters. The thermal structure of the IC gas is also assumed to be radially symmetric. Together these assumptions make possible the

determination of  $f_n$  and  $f_T$  from the observed X-ray surface brightness as a function of X-ray energy.

Because  $\Lambda(E, T_e)$  and  $\Psi(x, T_e)$  are non-linear functions of the temperature, the shapes of the X-ray and S-Z surface brightness profiles depend not only on the temperature form factor but also on its reference value. In general, the form factors cannot be determined from monochromatic imaging data if the cluster gas is not isothermal. However, at energies much lower than the electron thermal energy (as in the ROSAT/PSPC energy band), the X-ray emissivity of the IC gas depends weakly on the IC gas temperature. Therefore, even for a non-isothermal IC gas, a good approximation to the density form factor can be determined from the X-ray surface brightness profile.

The S-Z surface brightness is roughly proportional to the electron pressure integrated along the line of sight through the cluster. It is possible to constrain spherically symmetric models for  $f_T$  by integrating the product of  $f_n$  (determined consistently from the X-ray data for each  $f_T$  model) and  $f_\Psi(x, T_e)$  along the line of sight to determine a model for the S-Z surface brightness, which is then fit to the 2.1 mm data. In Section 7., we use this method to constrain models for the IC gas thermal structure. Presently, much stronger constraints on the thermal structure are determined from the spatially resolved X-ray spectra obtained by the ASCA satellite.

### 3. X-ray Analysis

A2163 was the target of pointed observations by the GINGA and ROSAT satellites. A detailed combined analysis of these observations has been published previously (Elbaz *et al.* 1995). The ROSAT/PSPC and GINGA spectra were simultaneously fit to a redshifted isothermal plasma emission model where the hydrogen column density along the line of sight ( $N_H$ ), heavy metal abundance, total emission measure, and IC gas temperature were free parameters. The best fit emission weighted temperature was found to be  $T_e = 14.6_{-8}^{+9}$  keV, at 90% confidence (Elbaz *et al.* 1995).

The ROSAT/PSPC data were used to determine the spatial dependence of the X-ray emission. In Fig. 2, we show the X-ray surface brightness as determined by the PSPC. The peak surface brightness was found at  $16^{\text{h}} 15^{\text{m}} 46^{\text{s}}$ ,  $-06^{\circ} 08' 55''$  (J2000). The radial profile of the surface brightness (corrected for

vignetting) was found by summing annuli about this central value, with significant emission detected up to  $18'$ . The surface brightness profile was fit with the combination of an isothermal  $\beta$  model (equation 22) convolved with the instrument point spread function (PSF) and a constant background. The best fit density model parameters were found to be  $\beta = .62_{-.02}^{+.015}$  and  $\theta_c = 1.20 \pm 0.075'$  at 90% confidence (Elbaz *et al.* 1995).

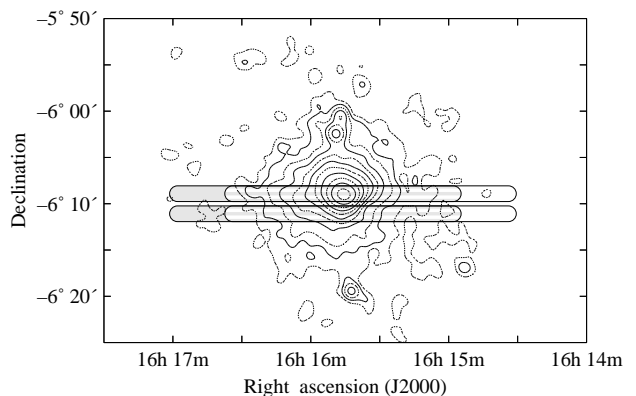


Fig. 2.— X-ray image of the A2163 cluster observed with the ROSAT/PSPC and corrected for vignetting. The contour levels are logarithmically spaced with the peak brightness corresponding to  $9.4 \times 10^{-2}$  cts arcmin $^{-2}$ . Superimposed are the SuZIE drift scans made in 1994; one row of detectors passes over the X-ray center and the other  $2.2'$  to the south. Scans were alternately begun  $12'$  (shaded) and  $18'$  ahead of the X-ray cluster.

Using the ASCA satellite it is, in principle, possible to measure large-scale variations in the temperature of the IC gas. Combining the ASCA/SIS+GIS spectra with the ROSAT/PSPC derived density model, Markevitch *et al.* (1996) determined the temperature of the IC gas in three radial bins of  $0 - 3$ ,  $3 - 6$ , and  $6 - 13$  X-ray core radii to be  $12.2_{-1.2}^{+1.9}$  keV,  $11.5_{-2.9}^{+2.7}$  keV, and  $3.8_{-0.9}^{+1.1}$  keV at 90% confidence.

As noted by Markevitch *et al.* (1996), the ASCA determined temperature is systematically lower than that found by GINGA. The emission-weighted ASCA/GIS+SIS average temperature for the combination of the 3 radial bins is  $\bar{T}_e = 11.2 \pm 1.1$  keV at 90% confidence (Markevitch, private communication), while an analysis of the GINGA data gives  $\bar{T}_e = 14.6_{-8}^{+9}$  keV, also at 90% confidence (Elbaz *et al.* 1995). These two temperature determinations

are inconsistent at 99.99% confidence. It is beyond the scope of this paper to try to understand the origin of this discrepancy, part of which may originate in the calibration of the instrument effective areas.

In Section 3.2., we estimate the uncertainty in the central and emission-weighted average temperatures of the IC gas taking this systematic difference into account. In addition, we discuss the effect of the uncertainty in temperature on the other X-ray parameters relevant for the determination of the Hubble constant. In Section 3.1., we consider the ASCA determined thermal structure and introduce a simple two parameter model for the IC gas temperature profile. In Section 3.3.3., we repeat the analysis of the ROSAT imaging data consistent with each of the models for the large scale thermal structure. We also determine the uncertainties on the X-ray normalization and density profile parameters due to systematic errors in the background and uncertainties in the cluster extent, which were not considered in Elbaz *et al.* 1995.

### 3.1. Temperature Profile

Independent constraints on the IC gas thermal structure can be derived from the combination of the X-ray derived density distribution and S-Z surface brightness. To facilitate this, we parameterize the thermal structure in terms of a hybrid model for the radial temperature profile of the IC gas. The model consists of an isothermal central region extending to  $\theta_{iso}$  beyond which the temperature decreases according to a polytropic model with index  $\gamma$ ,

$$T_c(\theta) = \begin{cases} T_{iso} & \theta \leq \theta_{iso} \\ T_{iso} \left[ \frac{1+(\theta/\theta_c)^2}{1+(\theta_{iso}/\theta_c)^2} \right]^{-\frac{3}{2}\beta(\gamma-1)} & \theta > \theta_{iso}. \end{cases} \quad (23)$$

This model was originally introduced by Hughes *et al.* (1988) in their study of the Coma cluster which was, prior to ASCA, the only cluster for which the radial temperature profile had been measured at large distances from the cluster center. In Coma, the IC gas temperature decreases significantly at large radii. In the analysis of EXOSAT, Tenma, and GINGA data for the Coma cluster, Hughes *et al.* (1993) set  $\gamma = 1.55$  and determined a best fit isothermal angular radius  $\theta_{iso} \approx 3.5\theta_c$ . We have generalized this model by allowing both  $\gamma$  and  $\theta_{iso}$  to vary.

This parametric model provides a convenient analytical description of the temperature profile measured by ASCA. In Fig. 3, we plot the approximate

68% confidence interval for the hybrid model parameters  $(\gamma, \theta_{iso})$  allowed by the ASCA data. These parameters are constrained by computing the emission-weighted average temperature in the three ASCA radial bins for each of the hybrid models considered. We determine the  $\chi^2$  for the fit of the models to the measured ASCA/GIS+SIS temperatures, leaving the central temperature as a free parameter. A range of model parameters for the thermal structure provide a good fit to the ASCA data; we adopt  $\theta_{iso} = 4.0\theta_c$  and  $\gamma = 2.0$  as representative values.

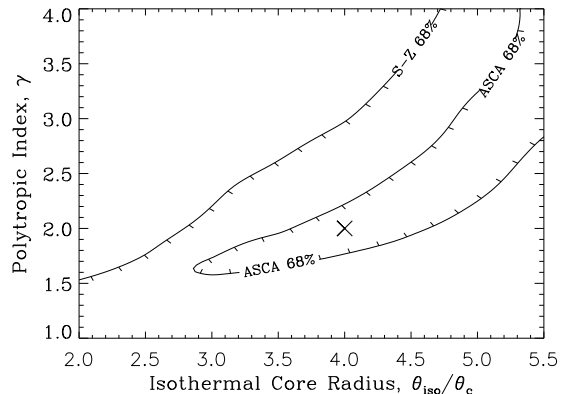


Fig. 3.— Fits of the ASCA and S-Z data to the hybrid thermal models. The hatched regions contain the allowed values of the model parameters at 68% confidence. The ROSAT fits constrain  $\gamma < 2.5$ , especially for small  $\theta_{iso}$ . The “X” marks the adopted hybrid model.

### 3.2. Central and Average Temperature

The discrepancy between the ASCA and GINGA determined temperatures makes the comparison of the isothermal and non-isothermal treatments difficult. In this section, we attempt to remedy this situation by determining a consistent X-ray temperature from the two experiments.

Markevitch *et al.* (1996) simultaneously fit the ASCA/SIS+GIS and GINGA spectra to determine 13.3, 13.3, and 3.8 keV in the three radial bins defined in Section 3.. For the analysis including the thermal structure, we adopt  $T_{e0} = 13.3$  keV as the central IC gas temperature. We determine the uncertainty of the central temperature taking into account systematic difference between the two experiments. Crudely scaling the error bars of the ASCA/GIS+SIS

central temperature to 68% confidence, we find  $T_{e0} \approx 12.2^{+1.2}_{-0.7}$  keV. Assuming the thermal structure determined by ASCA, the central temperature is  $\sim 7\%$  higher than the isothermal value. In this case, the central temperature determined by GINGA increases to  $T_{e0} \approx 15.6^{+0.6}_{-0.6}$  keV. We adopt error bars for the combined GINGA and ASCA temperatures that enclose the 68% confidence intervals from each of the experiments considered individually: ASCA ( $T_{e0} \gtrsim 12.2 - 0.7$ ) and GINGA ( $T_{e0} \lesssim 15.6 + 0.6$ ). Therefore, assuming the ASCA determined thermal structure, we find  $T_{e0} \approx 13.3^{+2.9}_{-1.8}$  keV at 68% confidence. In Section 7., we use this value of the temperature to determine  $H_0$  under the assumption of the ASCA thermal structure.

We also determine a consistent temperature for the case in which the IC gas is assumed to be isothermal. Using the ASCA+GINGA central temperature and the the ASCA/GIS+SIS thermal gradient, we estimate the emission-weighted average temperature to be  $\bar{T}_e \approx 12.4$  keV. The ASCA/GIS+SIS emission-weighted temperature is  $\bar{T}_e \approx 11.2 \pm 0.7$  keV at 68% confidence. We adopt error bars for the combined GINGA and ASCA analysis that enclose the 68% confidence intervals from both the ASCA ( $\bar{T}_e \gtrsim 11.2 - .7$  keV) and GINGA ( $\bar{T}_e < 14.6 + 0.6$  keV) isothermal spectral analysis. Therefore, assuming the IC gas to be isothermal, we find  $\bar{T}_e \approx 12.4^{+2.8}_{-1.9}$  keV at 68% confidence. In Section 6., we use this value of the temperature to determine  $H_0$  assuming the IC gas to be isothermal.

### 3.2.1. X-ray Emissivity

The temperature uncertainty contributes to the uncertainty of the central specific emissivity ( $\Lambda_{e0}$ ) in equation 21.  $\Lambda_{e0}$  is obtained by convolving  $\Lambda(T_e, E)$  with the ROSAT/PSPC response (Elbaz *et al.* 1995). The emissivity varies by  $\Delta\Lambda_{e0}/\Lambda_{e0} = {}^{+2.5}_{-4.0}\%$  for  $T_{e0} = 13.3^{+2.9}_{-1.8}$  keV; similar errors are obtained for an isothermal plasma with  $\bar{T}_e = 12.4^{+2.8}_{-1.9}$  keV.

We have fixed  $N_H$  and the metallicity to their best fit values as determined by Elbaz *et al.* 1995 (as was done by Markevitch *et al.* 1996 in their ASCA analysis). However, there are uncertainties in these values; from the ROSAT/GINGA analysis,  $\log(N_H) = 21.22 \pm 0.03$  and the metallicity is  $0.4 \pm 0.1$  at 68% confidence. The corresponding uncertainties on  $\Lambda_{e0}$  are  $\pm 2.5\%$  and  $\pm 1\%$ , respectively. We have assumed that these additional uncertainties are independent

from the uncertainty in the temperature. In particular, the  $N_H$  value is constrained by the PSPC spectrum which is insensitive to the exact temperature.

Adding the uncertainties in quadrature, we obtain a statistical uncertainty in the central specific emissivity,  $\Delta\Lambda_{e0}/\Lambda_{e0} = {}^{+3.7}_{-4.8}\%$ . This uncertainty is correlated with the temperature uncertainty ( $\Lambda_{e0}$  decreases with increasing temperature) and is included in the uncertainty in  $H_0$  due to variations in temperature.

## 3.3. X-ray Surface Brightness Analysis

### 3.3.1. Isothermal Model

The normalizations ( $N_X$ ,  $N_{SZ}$ ) and the density model parameters ( $\beta$ ,  $\theta_c$ ) are correlated. The term,  $N_{SZ}^2/N_X$ , which appears in equation 21, must be determined consistently from the X-ray and S-Z data. The statistical precision and spatial resolution of the X-ray imaging data for A2163 are much better than the corresponding precision in the S-Z data. As a result, the density profile shape is constrained by the X-ray surface brightness profile. The error on the peak Comptonization  $y_0$ , determined from the S-Z data, is dominated by the statistical errors on the S-Z data and not by the uncertainties in the density model parameters. We therefore express  $N_{SZ}^2/N_X$  in terms of the nearly independent quantities  $N'_X$  (determined from X-ray imaging data only) and  $y_0$ ,

$$\frac{N_{SZ}^2}{N_X} = \frac{y_0^2}{N'_X}, \quad (24)$$

where

$$N'_X = b_{X0} \frac{\Theta_{SZ0}^2}{\Theta_{X0}} = b_{X0} \theta_c \frac{B^2\left(\frac{1}{2}, \frac{3}{2}\beta - \frac{1}{2}\right)}{B\left(\frac{1}{2}, 3\beta - \frac{1}{2}\right)}, \quad (25)$$

$b_{X0}$  is the central X-ray surface brightness, and  $B$  is the incomplete beta function.

Because  $b_{X0}$  and the density model parameters are not independent, we directly compute the uncertainty in  $N'_X$  from fits to the original PSPC surface brightness profile obtained by Elbaz *et al.* (1995). A  $\chi^2$  procedure, as used in Avni (1976), is applied to determine the uncertainty with the other parameters ( $\beta$ ,  $\theta_c$ , and background level) being optimized for any given value of  $N'_X$ . We find the statistical uncertainty to be  $\Delta N'_X/N'_X = \pm 3.5\%$  at 68% confidence. The absolute calibration of the PSPC is uncertain by  $\sim \pm 5\%$ . Adding the uncertainties in quadrature, we determine the X-ray normalization to be uncertain by  $\Delta N'_X/N'_X = \pm 6.1\%$ . At 68% confidence,

the density model parameters are  $\beta = .616_{-.009}^{+.012}$  and  $\theta_c = 1.20 \pm 0.05'$ .

The derived density profile shape depends on the background level. The background level is a free parameter in the fit to the surface brightness profile and the statistical errors in the background are included in the uncertainties of the density model parameters. In the above analysis, variations of the background with position due to improper vignetting corrections and contributions from unresolved point sources (especially at the outer part of the field of view) are not taken into account. As discussed in Elbaz *et al.* 1995, these background variations are  $\sim 9\%$ . Squires *et al.* (1996) determined the effect of the background uncertainty on the determination of the density model by repeating the fits with the background  $\pm 10\%$  from the nominal value. The additional uncertainties in the model parameters are  $\Delta\beta = \pm 0.03$  and  $\Delta\theta_c = \pm 0.1'$ . The corresponding additional uncertainty on the structural form factor ( $\Theta_{SZ0}^2/\Theta_{X0}$ ) is  $\pm 2.5\%$ . Adding these systematic errors in quadrature with the statistical errors, we obtain  $\beta = .616 \pm 0.031$ ,  $\theta_c = 1.20 \pm .11'$ , and  $\Delta N'_X/N'_X = \pm 6.6\%$ .

### 3.3.2. Truncated Model

The isothermal  $\beta$  model (equation 22) is a good fit to the X-ray data within the radius of maximum detection ( $\theta_{max} = 15\theta_c$ ), at which the signal to noise ratio drops to unity (Elbaz *et al.* 1995). For values of  $\beta < 1.0$ , this simple model implies an infinite mass of IC gas. Therefore, at large radius, the density distribution of A2163 ( $\beta = .616$ ) must decrease more rapidly than the inferred density profile. One way to obtain a more realistic distribution is to assume that the gas density falls to zero at a cut-off radius ( $\theta_{cut}$ ) where  $\theta_{cut} \geq \theta_{max}$ . We have fit the X-ray data with models for the surface brightness due to a truncated density distribution for a range of cut-off radii,  $\theta_{max} \leq \theta_{cut} \leq \infty$ .

In the most extreme case ( $\theta_{cut} = \theta_{max}$ ), we find  $\beta = .625$  and  $\theta_c = 1.22'$ . These values are both within the 68% confidence intervals determined using the standard  $\beta$  model. The corresponding change in the X-ray normalization is  $N_X(\theta_{cut} = 15\theta_c)/N_X(\infty) = .98$ .

### 3.3.3. Hybrid Model

In the presence of thermal structure, the observed morphology of the X-ray surface brightness will be a

function of both the temperature of the IC gas and the energy band over which the measurement is made. We repeat the analysis of the ROSAT/PSPC data assuming models for the thermal structure given by equation 23.

We first compute the specific emissivity by convolving  $\Lambda(T_e, E)$  with the ROSAT/PSPC response in the considered energy band. A redshifted isothermal plasma model is used, where the hydrogen column density and the heavy metal abundance are fixed to their best fit isothermal values. Assuming values for the density and thermal model parameters, we then create a model for the X-ray surface brightness by numerically integrating equation 13. Each model, after convolution with the PSPC PSF and the addition of a constant background, is fit to the observed surface brightness profile. For a given thermal model, we then determine the best fit density model parameters and X-ray normalization, by minimizing the  $\chi^2$  of the model fit. We have done this for a grid of hybrid thermal models described by the parameters ( $\theta_{iso}, \gamma$ ). For the adopted thermal model ( $\gamma = 2.0$  and  $\theta_{iso} = 4.0\theta_c$ ), we determine  $\beta = 0.640$  and  $\theta_c = 1.26'$ . These values are listed, along with the isothermal model parameters in Table 1. In Section 7., each model for the thermal structure is combined with its corresponding ROSAT/PSPC derived density profile in order to determine a consistent model of the S-Z surface brightness.

The changes in the best fit density profile parameters are, for most models considered, smaller than the corresponding statistical uncertainties. However, for all models with values of  $\gamma > 2.5$ , especially those with small  $\theta_{iso}$ , the fit to the PSPC surface brightness is bad. The temperature reaches such a low value that the X-ray emission in the PSPC band cuts off sooner than the observed surface brightness distribution. This constrains the acceptable temperature model parameters to lie within the range plotted in Fig. 3.

## 4. S-Z Observations

### 4.1. Instrument

All S-Z observations were made using the Sunyaev-Zel'dovich Infrared Experiment (SuZIE) bolometer array at the Caltech Submillimeter Observatory (CSO) on Mauna Kea. A detailed description of the SuZIE instrument has been presented elsewhere (Holzapfel *et al.* 1996a). SuZIE is a  $2 \times 3$  array of



Temperature and Density Model Parameters

Thermal Structure	$kT_{e0}$ [keV]	$\gamma$	$\theta_{iso}[\theta_c]$	$\beta$	$\theta_c$
Isothermal	$12.4_{-1.9}^{+2.8}$	1.0	—	0.616	1.20
Truncated	$12.4_{-1.9}^{+2.8}$	$\infty$	15.0	0.625	1.22
Hybrid(ASCA)	$13.3_{-1.8}^{+2.9}$	2.0	4.0	0.640	1.26

Table 1: Temperature and density model parameters for the isothermal, truncated, and hybrid models.

300 mK bolometric detectors optimized for the observation of the S-Z effect in distant ( $z > .1$ ) clusters of galaxies. A tertiary mirror re-images the Cassegrain focus of the telescope to an array of parabolic concentrators which couple the radiation to the six individual composite bolometers (Alsop *et al.* 1992). In order to reduce spill-over, a 2K stop limits the illumination of the CSO 10.4m primary mirror to 50% of its total area. The array consists of two rows separated by 2.2'; each row consists of three co-linear array elements separated by 2.3'. Each array element produces a beam on the sky which is approximately 1.75' FWHM.

The spectral response of the array elements is determined by a common set of metal-mesh filters positioned between the parabolic concentrators and the cold stop. The filters can be changed for observations in several mm-wavelength passbands. The 2.1 mm filter passband is designed to maximize the ratio of the S-Z signal to the sum of the atmosphere and detector noise and has a FWHM  $\Delta\lambda/\lambda = .11$ .

Array elements within each of the two rows are electronically differenced by placing pairs of detectors in AC biased bridge circuits. The output of each bridge is synchronously demodulated to produce a stable DC voltage proportional to the instantaneous brightness difference between the two array elements. The electrical bias on each detector is adjusted so that the responsivities of the three detectors in each row are matched (Glezer *et al.* 1992). The bolometer differences strongly reject signals common to both elements, due to fluctuations in the temperature of the 300 mK heat sink and atmospheric emission. Each row produces three differences, two with beams separated by 2.3' and one with a 4.6' separation. During all observations, the telescope is fixed in place and the rotation of the earth drifts the source across the array of detectors. Keeping the telescope fixed while taking data eliminates signals due to modulation of

the telescope's sidelobes and microphonic response of the detectors. Between scans, the array is rotated about the optical axis so that the two rows of the array are kept parallel to the direction of the scan. The difference signal from each pair of detectors and the absolute voltage on each of the detectors is low-pass filtered at 2.25 Hz and digitally sampled at 5 Hz.

#### 4.2. Observations

A2163 was first observed on the nights of April 23-26, 1993 for a total of 16 hours of integration at 2.1 mm; these observations have been described in W94. W94 did not include the data from the night of April 23 in their analysis due to the short observation time and comparatively poor quality of the data. We include these results in this reanalysis, however, they make almost no contribution to the weighted mean. We observed A2163 at 2.1 mm on the nights of 1994 April 4, 9, 10 and 11 for a total of 8 hours. The array was positioned so one row passed over the X-ray center as determined by the ROSAT/PSPC (Elbaz *et al.* 1995), while the second row passed 2.2' in declination to the south. Scans were 30' long and begun at a Right Ascension Offset (RAO) leading the source by either 12' or 18'. In Fig. 2, we show a schematic of the 1994 scan strategy overlaid on the measured X-ray surface brightness contours. First, the telescope is pointed to a position leading the source by one of the two fixed RAOs. The telescope tracks this position while the data from the last scan is compressed and stored, the receiver is rotated, and the computers perform housekeeping chores. After about 10s, the telescope stops tracking and a new scan begins; while gathering data, the telescope is held fixed. At the end of the scan, the telescope is reset to the alternate RAO and the cycle is repeated. As is described in Section 5.3.4., alternating the RAO between sequential scans provides a sensitive test for instrumental baselines.

Over the course of the observations, the zenith angle of A2163 ranged from  $50^\circ$  to  $57^\circ$ . The optical depth of the atmosphere at the CSO was simultaneously measured with a tipping radiometer operating at 225 GHz. Converted to the frequency and zenith angle of these measurements, the atmospheric absorption ranged from 2 – 4% over the course of the observations and has been corrected for in the calibration of the data.

As a test for a possible instrumental baseline we observed regions free of known sources, selected so they could be observed over a similar range of hour angle and zenith angle as A2163. The 1993 observations were coupled with 6.7 hours of integration on a patch of sky centered at  $13^{\text{h}} 11^{\text{m}} 29^{\text{s}}$ ,  $-1^\circ 20' 11''$  (J2000). In 1994, we accumulated 8.5 hours of data on patch #1 centered at  $10^{\text{h}} 24^{\text{m}} 25^{\text{s}}$ ,  $3^\circ 49' 12''$  (J2000), and 7.5 hours on patch #2 centered at  $16^{\text{h}} 32^{\text{m}} 44^{\text{s}}$ ,  $5^\circ 49' 41''$  (J2000).

### 4.3. Calibration

In April 1993, scans of Jupiter, Saturn, Mars, and Uranus were made in order to map the beam shapes of the instrument and calibrate its responsivity. In W94, Mars was used as the primary calibration source. The scans of Mars were made with the receiver rotated by an angle somewhat larger than that used in the source observations. We have reanalyzed the April 1993 observations using Uranus for the calibration. The scans across Uranus were made with a receiver rotation angle of  $10^\circ$  which this lies near the center of the range of rotation angles under which A2163 was observed. This reduces the uncertainty in calibration due to changes in beam shape with receiver rotation.

In April 1994, both Uranus and Jupiter were available as calibration sources. As in the reanalysis of the 1993 data, Uranus was used both to map the beams and as the primary responsivity calibrator. The beam-shapes measured with Jupiter and Uranus exhibited a small and reproducible dependence on the rotation angle of the instrument about the optical axis. Over the course of the A2163 observations, the rotation angle varied from  $-45^\circ$  to  $+37^\circ$ . The calibrated models computed for the range of rotation angles differ by  $< 5\%$ .

In order to calibrate the data, we determine the ratio of the S-Z brightness to the brightness of the calibrator. The brightness of Uranus is found from a third order polynomial fit to the measured bright-

ness temperature as a function of wavelength (Griffin & Orton 1993). They assign an uncertainty of  $\pm 6\%$  to the brightness of Uranus, most of which arises from the  $\pm 5\%$  uncertainty in the absolute brightness of Mars from which Uranus is calibrated. The spectral response of the array elements, including detailed checks for out of band leaks, have been measured using a Fourier transform spectrometer. The central frequencies of the six array elements are determined with an absolute accuracy of better than 1% and exhibit a reproducible scatter of less than 1% about the mean (Holzapfel *et al.* 1996a). Including uncertainties in the spectral calibration, measured beam-shapes and absolute brightness of Uranus, the uncertainty in the absolute calibration of the instrument responsivity to the thermal S-Z effect is estimated to be  $\pm 8\%$ .

## 5. 2.1mm Analysis

### 5.1. S-Z Data Set

Each of the two rows consists of three detectors:  $s_1$ ,  $s_2$ , and  $s_3$ . Detector signals are differenced in pairs (in hardware) to form three difference signals:  $d_{12} = s_1 - s_2$ ,  $d_{23} = s_2 - s_3$ , and  $d_{31} = s_3 - s_1$ . These differences correspond to angular chops of  $2.3'$ ,  $2.3'$ , and  $4.6'$  respectively. Each detector contributes to two of the difference signals, therefore, the three detector differences are not independent. To remove the degeneracy, the two  $2.3'$  differences are differenced to form a triple beam chop,

$$t_{123} = d_{12} - d_{23} = s_1 - 2s_2 + s_3. \quad (26)$$

This combination of detector signals has the added benefit of being insensitive to linear changes in brightness across the array, and therefore provides superior sensitivity in the presence of varying atmospheric emission. The data set consists of 4 difference signals:  $d_{31}$ ,  $t_{123}$ ,  $d_{64}$ , and  $t_{456}$  corresponding to the  $4.6'$  difference and triple beam chop for each of the two rows of detectors. From now on, we refer to these four difference signals as  $d_k$ , where  $k$  ranges from 1 to 4. The average signal of the undifferenced detectors is also computed,

$$s = \frac{1}{6} \sum_k^6 s_k. \quad (27)$$

We use the average single detector signal as a monitor of the absolute atmospheric emission and to correct any residual common-mode response of the detector differences.

We clean the raw data of transients due to the interaction of cosmic rays with the detectors. The bolometer and electronic time constants are fast enough that the system recovers within  $< 1$  s. These transients are identified using an algorithm that computes the derivative of the data in the scan and then looks for the large positive and negative slopes associated with a cosmic ray event. Less than 5% of the data are identified as contaminated by cosmic rays. The raw data are then binned into 3 s bins corresponding to 15 5 Hz samples or  $0.75'$   $\cos\delta$  on the sky. Samples flagged as bad due to cosmic rays are left out when the bin averages are computed; bins with less than 8 samples are not included in the analysis.

## 5.2. S-Z Surface Brightness Model

The computed S-Z surface brightness profile of A2163 is  $\sim 5'$  FWHM, greater than the largest beam-throw of SuZIE, which is  $4.6'$ . In order to accurately determine the central surface brightness, we must simulate the observation of an extended source.

A model for the surface brightness of the S-Z thermal component is computed from the X-ray surface brightness determined density profile and the assumed thermal structure.

$$I_{SZ\nu}(\theta, \phi) \propto \int f_n f_\Psi(x, T_e) d\xi \quad (28)$$

We express the surface brightness morphology in terms of a dimensionless form factor,

$$S_i(\theta, \phi) = \frac{I_{SZ\nu_i}(\theta, \phi)}{I_{SZ\nu_i}(0, 0)} = \frac{\int f_n(\theta, \phi, \xi) f_\Psi_i(\theta, \phi, \xi) d\xi}{\int f_n(0, 0, \xi) f_\Psi_i(0, 0, \xi) d\xi}, \quad (29)$$

where  $S_i$  (in order to take relativistic corrections into account) is evaluated at the S-Z intensity weighted band center for each array element. The surface brightness model ( $S_i$ ) is convolved with the single detector beam-maps constructed from scans over planets ( $V_{P_i}$ ) to generate a model for the response of the detector signals,

$$sm_{K,T_i}(\theta) = \frac{\Delta I_{SZi}}{I_{P_i}} \frac{1}{\Omega_P} \int V_{P_i}(\theta - \theta', \phi') S_{K,T}(\theta', \phi') d\theta' d\phi', \quad (30)$$

where  $\Omega_P$  is the solid angle subtended by the planetary calibrator. The ratio of the relativistically correct S-Z brightness to the brightness of the planet is

$$\frac{I_{SZi}}{I_{P_i}} = \frac{\int f_i(\nu) I_{SZ\nu} d\nu}{\int f_i(\nu) I_{P\nu} d\nu}, \quad (31)$$

where  $f_i(\nu)$  is the measured spectral response of each array element and  $I_{P\nu}$  is the intensity of the planetary calibrator.

The models for the response of the array elements are differenced to create models for the response of the detector differences. The  $\sim .05'$  resolution differential source model is binned identically to the scan data to determine the model signal for each of the  $\sim .75'$  data bins. The source models are then designated as  $m_{ki}(RA)$ , where  $k$  is one of the four detector differences,  $i$  is the position (by bin number) in the scan, and RA is a offset of the model from the nominal X-ray determined position.

## 5.3. Peak Comptonization and Uncertainties: Isothermal Model

### 5.3.1. Coadded Data Analysis

We coadd the difference signals over many scans to create a high sensitivity scan of the differential surface brightness as a function of RA. For each difference signal ( $k$ ) and scan ( $j$ ), we clean the data by removing the best fit linear baseline,

$$x_{kji} = d_{kji} - a_{kj} - i b_{kj}. \quad (32)$$

The value of each coadded bin  $i$  ( $x_{ki}$ ) is given by the weighted sum of its values in each of  $N_s$  scans,

$$x_{ki} = \frac{\sum_{j=1}^{N_s} \frac{x_{kji}}{\text{RMS}_{kj}^2}}{\sum_{j=1}^{N_s} \frac{1}{\text{RMS}_{kj}^2}}. \quad (33)$$

Each bin is weighted by the residual RMS of the scan with the best fit (minimum RMS) linear baseline removed,

$$\text{RMS}_{kj}^2 = \frac{\sum_{i=1}^{N_b} x_{kji}^2}{(N_b - 1)}, \quad (34)$$

where  $N_b$  is the number of bins in a scan. The uncertainty in the value of each bin is determined from the weighted dispersion of that bin for each scan about the mean of  $N_s$  scans,

$$\sigma_{ki} = \sqrt{\frac{\sum_{j=1}^{N_s} \frac{(x_{ki} - x_{kji})^2}{\text{RMS}_{kj}^2}}{(N_s - 1) \sum_{j=1}^{N_s} \frac{1}{\text{RMS}_{kj}^2}}}. \quad (35)$$

The coadded scans are fit with the isothermal source model determined in Section 5.2.. The best fit source amplitude ( $y_0$ ) and position ( $RA$ ) are found by minimizing the  $\chi^2$  of the fit to all four difference signals to the appropriate differential source models,

$$\chi^2 = \sum_{k=1}^4 \sum_{i=1}^{N_b} \frac{(x_{ki} - y_0 m_{ki}(RA) - a_k - i b_k)^2}{\sigma_{ki}^2}, \quad (36)$$

where the sum over  $k$  is for all the difference signals. This procedure accurately determines the source amplitude, so long as the signal is a small contribution to the structure in the individual scans. If the source contributes significantly to the structure in a single scan, a scan with less signal will have lower RMS and will be weighted higher in the coadd. Coadding the scans using equations 32–34 could introduce a bias in the amplitude of the coadded scans. However, the position determined from the coadded data should be accurate. Once the source position is known, we can repeat the analysis in a way that takes the contribution of the source to the scan weighting into account.

The construction of the coadded scans is repeated with the bins weighted by the residual RMS of the scans after the removal of the best fit source model, residual common-mode signal, and linear baseline,

$$\text{RMS}_{kj}^2 = \frac{\sum_{i=1}^{N_b} (d_{kji} - y_{kj} m_{ki}(RA) - \alpha_{kj} s_{ji} - a_{kj} - i b_{kj})^2}{(N_b - 1)}. \quad (37)$$

Allowing the source model to vary, while determining the weights, ensures that the weighting does not bias the signal amplitude. In Appendix A., we discuss the removal of the residual common-mode signal and demonstrate that it has no systematic effect on the fit results. We then coadd the binned scans with the best fit linear baseline and residual common-mode signal removed,

$$x_{kji} = d_{kji} - \alpha_{kj} s_{ji} - a_{kj} - i b_{kj}. \quad (38)$$

Using equations 33 and 35, we recompute the bin averages and uncertainties which are free of bias due to the non-zero source amplitude. In Fig. 4, we show coadded data scans for the 1994 observations of A2163 and a patch of blank sky.

The determination of accurate uncertainties for the coadded scan fits is difficult due to the presence of

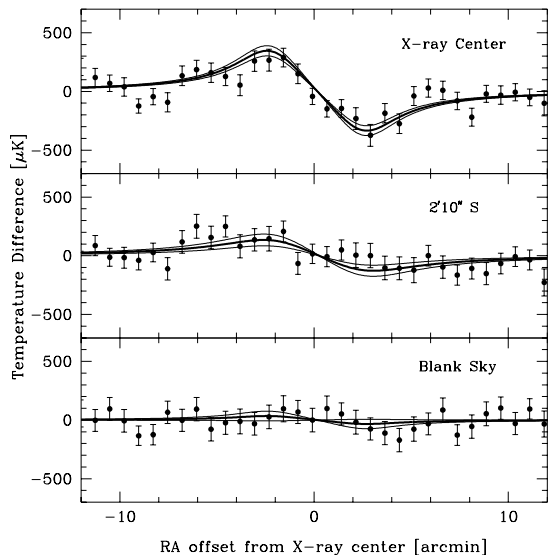


Fig. 4.— Coadded 4.6′ difference data for scans across the X-ray center of A2163, 2.2′ to the south, and region #2 of the 1994 “blank sky”. The data is plotted in terms of a Rayleigh-Jeans temperature difference completely filling one of the beams. The heavy curve is the best fit isothermal model to the 4.6′ and TBC data, and the light curves correspond to the  $\pm 1\sigma$  uncertainties on the model amplitude.

atmospheric emission which results in noise correlated between bins and detector differences. In Section 5.3.2., we use the fact that the noise from one scan to the next is uncorrelated to determine the uncertainty in the total data set and provide an accurate calibration of the uncertainty in the coadded fits.

### 5.3.2. Single Scan Fits

Once the source position is known, each scan can be used as an independent measurement of the source amplitude. The source amplitude for each scan is found by minimizing the  $\chi^2$  of the model fit to the desired data scans,

$$\chi_j^2 = \sum_k \sum_{i=1}^{N_b} \frac{(d_{kji} - y_{0j} m_{ki}(RA) - \alpha_{kj} s_{ji} - a_{kj} - i b_{kj})^2}{\text{RMS}_{kj}^2}, \quad (39)$$

where  $\text{RMS}_{kj}$  is given by equation 38. The uncertainty in the peak Comptonization ( $\sigma_{y_{jj}}$ ) is simply the change in  $y_{0j}$  corresponding to  $\Delta\chi_j^2 = 1$ . We

determine the mean peak Comptonization for a given observation by averaging the values  $y_{0j}$  for each of the  $N_s$  scans weighted by  $\sigma_{yj}$ ,

$$y_0 = \frac{\sum_{j=1}^{N_s} \frac{y_{0j}}{\sigma_{yj}^2}}{\sum_{j=1}^{N_s} \frac{1}{\sigma_{yj}^2}}. \quad (40)$$

The weighted dispersion of the scan amplitudes about the mean is used to estimate the uncertainty in the determination of the mean for each observing period,

$$\sigma_y = \sqrt{\frac{\sum_{j=1}^{N_s} \frac{(y_0 - y_{0j})^2}{\sigma_{yj}^2}}{(N_s - 1) \sum_{j=1}^{N_s} \frac{1}{\sigma_{yj}^2}}}. \quad (41)$$

In Fig. 5, we show a histogram of the peak Comptonization results for simultaneous fits to both array rows for every A2163 scan taken in 1993 and 1994. The mean and width of this distribution can be used to determine the peak Comptonization and uncertainty in the simple case when all scans are weighted equally. Using this method, the mean is unchanged while the uncertainty in  $y_0$  is  $\sim 30\%$  higher than that found when the scan amplitudes are weighted using equation 41. We do not use the results of this simple analysis, however, it illustrates the independence of the results from the details of the analysis.

For each night, RAO, and scan declination, we use equations 39–41 to compute the mean amplitude and uncertainty; these results are listed in Table 2. The single scan amplitudes are combined to determine an average peak Comptonization for all the data at each of the three scanned declinations; these results are listed at the bottom of the columns in Table 2. Due to correlated sky noise, the results of the fits to each of the two rows are not independent. In order to estimate the uncertainty of the total data set, we simultaneously fit to the signals from both rows. Assuming the sky noise between scans to be uncorrelated, we use equations 40 and 41 to determine  $y_0 = 3.73 \pm .35 \times 10^{-4}$ .

The average source amplitudes determined by the single scan fits agree with the results of the fits to the coadded data, while the uncertainties are a factor of 1.4 to 2.0 higher than those determined from the fits to the coadded data. This is because the atmospheric

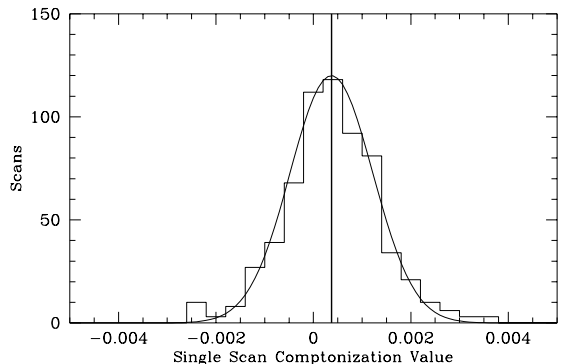


Fig. 5.— Histogram of peak Comptonization values from simultaneous fits to all four differential signals in each individual scan. The distribution is well approximated by the superimposed Gaussian, the mean is marked with a vertical line.

noise, which dominates the noise in the scans, is correlated between difference signals and bins in a given scan. In order to use the coadded data to determine confidence intervals for the position and morphology of the S-Z surface brightness, we must take the correlation of the noise into account. To do this, we scale the uncertainties of the coadded bins so that the uncertainty in the coadded scan amplitude is the same as that from determined the single scan fits. The scaling factor is insensitive to the details of the cluster position and morphology. We can then use the coadded data to determine the confidence intervals for parameters such as the model position which cannot be determined from the individual scan fits. All fits to coadded data discussed in this paper are for data with bin uncertainties scaled to compensate for correlated noise.

### 5.3.3. Peak S-Z Surface Brightness Position

With the coadded scan bin uncertainties appropriately scaled, we use a maximum likelihood indicator to determine confidence intervals in the model amplitude and position. We determine the position of the

Peak Comptonization $\times 10^4$ in A2163: Isothermal Model				
Date	RAO	$\Delta\delta = 0'$	$\Delta\delta = +2'10''$	$\Delta\delta = -2'10''$
Peak Comptonization, $y_0 \times 10^4$				
1993 April 23	16.5'	$0.72 \pm 2.78$	$-3.34 \pm 4.64$	...
	22.5'	$2.52 \pm 2.15$	$9.33 \pm 6.36$	...
1993 April 24	16.5'	$5.06 \pm 1.39$	$7.33 \pm 2.36$	...
	22.5'	$3.40 \pm 1.66$	$0.51 \pm 2.32$	...
1993 April 25	8.5'	$4.46 \pm 1.17$	$1.74 \pm 2.26$	...
	14.5'	$3.30 \pm 1.22$	$4.96 \pm 2.20$	...
1993 April 26	8.5'	$4.39 \pm 0.82$	...	$1.32 \pm 2.32$
	14.5'	$6.71 \pm 1.08$	...	$2.03 \pm 2.48$
1994 April 4	12'	$5.38 \pm 2.42$	...	$11.43 \pm 7.33$
	18'	$7.01 \pm 1.20$	...	$15.11 \pm 5.59$
1994 April 9	12'	$3.20 \pm 0.77$	...	$3.58 \pm 2.20$
	18'	$2.41 \pm 0.83$	...	$1.67 \pm 2.61$
1994 April 10	12'	$3.08 \pm 1.65$	...	$-2.18 \pm 3.53$
	18'	$2.25 \pm 1.08$	...	$3.17 \pm 3.17$
1994 April 11	12'	$4.36 \pm 1.04$	...	$1.05 \pm 3.10$
	18'	$3.54 \pm 1.23$	...	$2.03 \pm 3.42$
Weighted mean		$3.87 \pm 0.35$	$3.50 \pm 1.10$	$2.77 \pm 0.97$

Table 2: Results of fits of the isothermal model to the data for each observation,  $\delta$ , and RA. The total results for each declination (bottoms of columns) are calculated in the same way as the individual sets using the distribution of the scan amplitudes.

peak S-Z surface brightness to be offset from the peak X-ray surface brightness by  $\Delta RA = +.35 \pm .14'$  at 68% confidence. The value of the peak Comptonization decreases by less than 1.0% from its value at the central position over the allowed range of RA.

We estimate the uncertainty in pointing the SuZIE instrument to be  $\lesssim 10''$ . ROSAT astrometry is typically uncertain by  $10 - 15''$ , unless special care has been taken to locally align X-ray and optical frames. Because no X-ray bright optical sources were present in the ROSAT field, this was not possible for A2163. Including the uncertainty in the ROSAT and SuZIE pointing, the offset between the X-ray and S-Z peak surface brightnesses is then  $\Delta RA = +.35 \pm .33'$  at 68% confidence.

We do not have sufficient coverage to accurately locate the peak S-Z surface brightness in declination. Assuming the peak S-Z and X-ray surface brightnesses to be coincident, the  $\delta$  of the peak surface brightness is uncertain by the quadrature sum of the ROSAT and SuZIE pointing uncertainties,  $\Delta\delta \approx .30'$ . If the true position of the peak surface brightness is offset from the declination of our scan, the measured

peak Comptonization will be smaller than the true value. Fitting the data to a model for scans offset in  $\delta$  from the peak surface brightness, we find that the peak Comptonization is  $\sim 2.0\%$  smaller for  $\Delta\delta = \pm .30'$ . The uncertainty in the position of the peak S-Z surface brightness, therefore, results in an uncertainty in the peak Comptonization,  $\Delta y_0/y_0 = +2.2\%$ . This contribution to the total uncertainty is listed under “Position” in Table 5.

#### 5.3.4. Baseline

We analyze the “blank sky” scans across regions of sky free of known sources (described in Section 4.2.) exactly as the source data, to test for an instrumental baseline. An instrumental baseline with the same temporal features as the source model would be detected as a non-zero Comptonization for these regions.

In the April 1993 observations, the RAO of sequential scans was alternated in the same way as the for the source data. In W94, this data was used to estimate the baseline contribution to the uncertainty in the source amplitude. Reanalyzing this data using the ROSAT density model and the resid-

ual common-mode signal subtracted scans, we find  $y_0 = -0.1 \pm 4.2 \times 10^{-5}$

In the April 1994 observations (patch #1 and patch #2), the RAO was alternated between 12' and 18' in sequential scans. The results of these observations have been used to place upper limits on arcminute scale CMB anisotropies (Church *et al.* 1996). Analyzing the baseline data in the same way as the source data, we find  $y_0 = 1.3 \pm 3.1 \times 10^{-5}$  and  $y_0 = 1.8 \pm 3.1 \times 10^{-5}$  for the two patches, respectively. In Fig. 4, we show the coadded 4.6' difference for the scans on patch #2. Combining the results from all three patches, we determine  $y_0 = 1.45 \pm 1.9 \times 10^{-5}$ , indicating no significant instrumental baseline. Combining the results from multiple patches reduces the signal from potential sources of confusion but should accurately determine the effect of any common instrumental baseline. One problem with this method is that the baseline data and source data, although gathered at similar azimuth and zenith angle, are not gathered simultaneously or even on the same evening. Any baseline signal, because it is not significant in a single scan, must be correlated in time between several scans. This does not guarantee the baseline will be constant over the course of an observation.

We have devised a method which allows us to use the source data to test for the presence of a scan-correlated baseline. Differencing scans taken adjacent in time at two different RAOs allows the subtraction of the common baseline with little effect on the expected signal. Each pair of scans are differenced by subtracting their raw 5 Hz sampled time streams. The data are then analyzed exactly as described in Sections 5.–5.3.4..

We construct a model for the differential surface brightness by differencing two models with the appropriate RAO difference between them. We choose the RAO difference (6') to be large enough so that the two models are well separated in the scan and therefore will not subtract much signal when differenced. The differenced model is then fit to the correlation corrected coadded scans in order to determine the source amplitude and position. Fitting to the isothermal model, we find  $y_0 = 3.49 \pm .40 \times 10^{-4}$  and  $\Delta RA = +0.19 \pm 0.18'$  at 68% confidence. These results agree, within the quoted statistical errors, with those determined from the undifferenced data.

The lack of any significant change when the scans are differenced, as well as the null result for the “blank sky” fields, indicates that there is no significant in-

strumental baseline with the same temporal dependence as the source model. The difference between the results of the fits to both RAOs and the differenced scans is treated as an additional contribution to the uncertainty in  $y_0$  and is listed under “Baseline” in Table 5. Including the additional uncertainty due to the possibility of an instrumental baseline, the results from Section 5.3.2. become  $y_0 = 3.73_{-.43}^{+.35} \times 10^{-4}$ .

#### 5.4. Density Model Uncertainties

We consider now the effect of the uncertainties in the density model on the determination of  $y_0$ . We have fit the S-Z data with the range of density models allowed by the X-ray analysis. The uncertainties in the density model parameters (Section 3.3.1.) contribute an uncertainty in the peak Comptonization of  $\Delta y_0/y_0 = {}_{-3.6}^{+2.5}$  % at 68% confidence. In W94, the data were fit with a template derived from the density model determined from the analysis of Einstein data:  $\theta_c = 1.15$  and  $\beta = 0.59$  (Arnaud *et al.* 1992). In this paper, these data are reanalyzed using the ROSAT/PSPC density model which results in a peak Comptonization lower by  $\sim 4\%$ .

The truncated density model, introduced in Section 3.3.2., is used to generate a model for the isothermal S-Z surface brightness. Fitting the measured S-Z surface brightness with the model for the truncated surface brightness, we find  $y_0(\theta_{max})/y_0(\infty) = .925$ . The angular scale factor ( $\Theta_{SZ}$ ) also decreases when the density model is truncated; this nearly compensates for the decrease in the measured peak Comptonization. Even in the most extreme case, the S-Z normalization is nearly independent of the presence of a density cut-off and  $N_{SZ}(\theta_{max})/N_{SZ}(\infty) = .985$ .

The uncertainty in the peak Comptonization due to the adopted density model is the sum of the uncertainties due to the uncertainty in the model parameters and the assumed functional form for the density profile. Adding these contributions to the uncertainty in quadrature, we determine  $\Delta y_0/y_0 = {}_{-8.3}^{+2.5}$  %. This analysis is performed assuming an isothermal IC gas; in the presence of thermal structure of the form discussed in Section 7., the effect of the cut-off density model will generally be smaller.

#### 5.5. Isothermal Temperature Uncertainty

Due to our use of the relativistically correct calculation of the Comptonization (Section 2.1.), the effective peak Comptonization derived from S-Z data

depends on the assumed temperature. For temperatures in the range allowed by the GINGA and ASCA spectral analysis (Section 3.2.),  $y_0 \propto T_e/\Psi$  changes by  ${}^{+1.6}_{-1.2}\%$ . Including uncertainties in the baseline, calibration, and density distribution and temperature of the IC gas, we determine  $y_0 = 3.73^{+.48}_{-.61} \times 10^{-4}$ .

## 6. Hubble Constant: Isothermal gas

Using equations 21, 7 and 25 we can express  $d_A$  in terms of the nearly independent quantities  $N'_X$ ,  $T_e$  and  $y_0$ ,

$$d_A = \frac{y_0^2}{N'_X} \left( \frac{m_e c^2}{kT_e} \right)^2 \frac{\Lambda_e}{4\pi(1+z)^3 \sigma_T^2}. \quad (42)$$

Apart from relativistic corrections, the errors in  $y_0$  and  $T_e$  can be considered as independent; the corresponding contributions to the total uncertainty for  $H_0$  are added in quadrature.

Assuming a standard  $\beta$  model, we determine the contribution of the uncertainty in the density model to the uncertainties in  $N'_X$  (Section 3.3.1.) and  $y_0$  (Section 5.4.). The change in  $y_0$  is small and has the same sign as the change in  $\Delta N'_X$ ; therefore,  $\Delta H_0/H_0 \approx \Delta N'_X/N'_X = \pm 6.6\%$  is an overestimate of the true uncertainty. This contribution to the uncertainty in  $H_0$  is listed in Table 6 under ‘‘X-ray normalization’’. Compared to the contributions due to the uncertainties in the S-Z and central temperature results, the contribution of the density model to the total uncertainty is nearly negligible. Taking only the uncertainties in the S-Z and X-ray normalizations into account, we determine  $H_0(q_0 = \frac{1}{2}) = 59.6^{+21.5}_{-13.1} \text{ kms}^{-1} \text{ Mpc}^{-1}$ .

In order to account for the systematic difference in the ASCA and GINGA temperatures, we use the estimated isothermal X-ray temperature determined in Section 3.2.. The uncertainty in  $H_0$  due to  $T_e$  includes the effect of the temperature uncertainty on  $\Lambda(T_e)$  as determined in Section 3.2.1.. In Table 3, we list the results for  $H_0$ , as a function of the assumed thermal structure and the included sources of uncertainty. Including the uncertainties in the S-Z and X-ray normalizations and X-ray temperature, we determine  $H_0(q_0 = \frac{1}{2}) = 59.6^{+40.7}_{-22.6} \text{ kms}^{-1} \text{ Mpc}^{-1}$ .

We also determine the effect of the truncated density model described in Section 3.3.2. on the value of  $H_0$ . Because  $N_{SZ}$  and  $N_X$  are insensitive to the details of the density model, so is the value of  $H_0$ ;

for the most extreme case ( $\theta_{cut} = \theta_{max}$ ), we find  $H_0(\theta_{max})/H_0(\infty) = 1.01$ . For the remainder of this paper we assume the IC gas density can be described by a standard  $\beta$  model with  $\theta_{cut} = \infty$ . Because the X-ray normalization contains the uncertainty due to density model parameters, the additional contribution to  $H_0$  is simply that due to the assumption of the density functional form,  $\Delta H_0/H_0 = +1.0\%$ . This contribution to the uncertainty in  $H_0$  is listed under ‘‘Density Model’’ in Table 6. This analysis is performed assuming an isothermal IC gas; in the presence of thermal structure of the form discussed in Section 7., the uncertainty due to the assumption of a cut-off density model will generally be smaller.

In Section 5.3.3., we determined the effect of the uncertainty in the position of the peak S-Z surface brightness on the value of  $y_0$ . The uncertainty in the position contributes an uncertainty to the Hubble constant of  $\Delta H_0/H_0 = -4.5\%$ ; this contribution to the total uncertainty is listed under ‘‘Position’’ in Table 6.

## 7. Large-scale Thermal Structure

In this Section, we repeat the determination of the Hubble constant under the assumption of a thermal structure of the form described by equation 23. As was outlined in Section 3.3.3., we repeat the analysis of the ROSAT surface brightness in order to rederive the density model parameters ( $\beta$ ,  $\theta_c$ ) for each set of thermal structure parameters ( $\gamma$ ,  $\theta_{iso}$ ). For the adopted hybrid model ( $\gamma = 2.0$ ,  $\theta_{iso} = 4.0\theta_c$ ), the reanalysis of the ROSAT data yields density parameters  $\beta = 0.640$  and  $\theta_c = 1.26'$ . Using equations 28–31 we combine the models for the IC gas temperature and density to create models for the S-Z surface brightness. Each model is fit to the coadded data scans in order to determine the peak Comptonization. In Fig. 3, we plot the 68% confidence interval in the  $(\theta_{iso}, \gamma)$  plane for fits to the coadded S-Z data. The S-Z measurements lack sufficient sensitivity to detect a thermal gradient of the type determined from recent ASCA results. The ratio of the peak Comptonization to that determined assuming an isothermal gas is plotted as a function of  $\theta_{iso}$  and  $\gamma$  in Fig. 6. For the range of temperature model parameters allowed by the ASCA results at 68% confidence (see Fig. 3), the values of the Comptonization span  $y_0/(y_0)_{iso} = .82 \pm .03$ . Using the procedure described in Section 5.3.2., we determine the peak Comptoniza-



Hubble Constant (Thermal Structure)			
$H_0$ [kms <sup>-1</sup> Mpc <sup>-1</sup> ]			
Thermal Structure	$N_X, N_{SZ}$	$N_X, N_{SZ}, T_{e0}$	Total
Isothermal	59.6 <sup>+21.5</sup> <sub>-13.1</sub>	59.6 <sup>+40.7</sup> <sub>-22.6</sub>	59.6 <sup>+45.3</sup> <sub>-30.9</sub>
Hybrid(ASCA)	78.4 <sup>+31.3</sup> <sub>-17.3</sub>	78.4 <sup>+53.8</sup> <sub>-27.9</sub>	78.4 <sup>+59.9</sup> <sub>-39.8</sub>

Table 3: The Hubble constant determined for both isothermal and hybrid thermal structure. The results are calculated for three different cases. In the first column under  $H_0$ , only uncertainties in the X-ray and S-Z normalizations are included. The second column includes the uncertainty in the IC gas central temperature. The third column includes additional uncertainties due to peculiar velocity, astrophysical confusion, clumped IC gas, and cluster asphericity.

tion from single scan fits to the hybrid S-Z surface brightness model to be  $y_0 = 3.07 \pm .29 \times 10^{-4}$ . The results of the fits at each declination are listed in Table 4.

Peak Comptonization & Uncertainty	
Source	Uncertainty
	$y_0 \times 10^4$
Statistical	$3.07 \pm .29$
Baseline	-.27
Calibration	$\pm .25$
Position	+.07
Density Model	$^{+.08}_{-.25}$
Thermal Gradient (ASCA)	$\pm .08$
Central Temperature	$^{+.05}_{-.04}$
	$3.07^{+.40}_{-.54}$
Peculiar Velocity	$\pm .23$
Radio Confusion	$^{+.25}_{-.05}$
Primary Anisotropies	$\pm .12$
Total	$3.07^{+.54}_{-.60}$

Table 5: Peak Comptonization and contributions to uncertainty using the adopted hybrid thermal structure.

We repeat this analysis for the RAO differenced data. The peak Comptonization from the single scan fits is  $y_0 = 2.80 \pm .32 \times 10^{-4}$ . We use the difference between this result and the peak Comptonization for

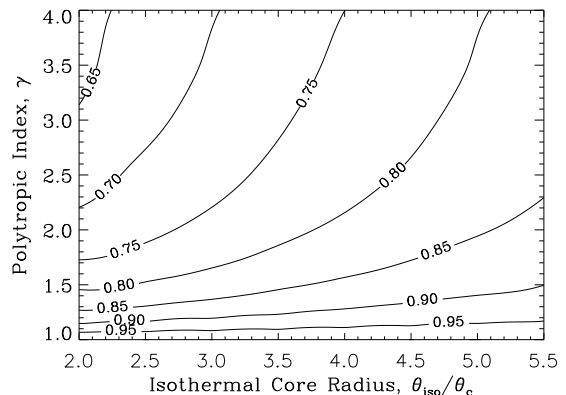


Fig. 6.— Ratio of the peak Comptonization to the isothermal value ( $y_0/(y_0)_{iso}$ ), plotted as a function of the hybrid thermal model parameters.

the undifferenced scans to estimate the baseline uncertainty. Combining the result of the fits to both RAOs with uncertainties in the baseline, calibration, and density and temperature models, we determine  $y_0 = 3.07^{+.40}_{-.54} \times 10^{-4}$ . The density model uncertainty is assumed to be the same as in the isothermal case (Section 6.). This is justified because the X-ray surface brightness profile is insensitive to the thermal structure for the considered range of thermal models. The individual contributions to the uncertainty in  $y_0$  are listed in Table 5.

We combine the X-ray and S-Z results to determine  $H_0$  as a function of the cluster thermal structure. In this analysis, we make one of two assumptions about the results of the X-ray observations. In the first case,

Peak Comptonization, $y_0 \times 10^4$				
Thermal Structure	$\Delta\delta = 0'$	$\Delta\delta = +2' 10''$	$\Delta\delta = -2' 10''$	Total
Isothermal	$3.87 \pm 0.35$	$3.50 \pm 1.10$	$2.77 \pm 0.97$	$3.73 \pm 0.35$
Hybrid(ASCA)	$3.16 \pm 0.32$	$3.34 \pm 1.19$	$2.21 \pm 0.91$	$3.07 \pm 0.29$

Table 4: Peak Comptonization at each declination for the cases when the IC gas is either isothermal or has the ASCA determined thermal structure. The uncertainties include statistical uncertainty only. The numbers under total are calculated from simultaneous fits to both rows of the array.

Hubble Constant & Uncertainty	
Source	Uncertainty $\text{kms}^{-1}\text{Mpc}^{-1}$
X-ray Normalization	$\pm 5.2$
S-Z Normalization	$+30.8$ $-16.5$
Position	$-3.5$
Density Model	$+0.8$
Thermal Gradient (ASCA)	$+1.5$ $-1.2$
Central Temperature	$+43.8$ $-21.9$
	$78.4^{+53.8}_{-27.9}$
Peculiar Velocity	$+13.0$ $-10.4$
Asphericity	$\pm 21.7$
Clumping	$-7.8$
Radio Confusion	$+2.6$ $-11.4$
Primary anisotropies	$+6.7$ $-5.9$
Total	$78.4^{+59.9}_{-39.8}$

Table 6: Hubble Constant and contributions to the uncertainty using the adopted hybrid thermal structure. The S-Z normalization includes uncertainties due to statistical uncertainty, baseline, and calibration.

we assume that the central temperature of the IC gas has been determined, this requires spatial resolution in the spectral measurement. For the allowed range of thermal models, we find  $N_X/(N_X)_{iso} = .96 \pm .02$  and  $N_{SZ}/(N_{SZ})_{iso} = .92 \pm .02$ . In Fig. 7, we plot the ratio of the true value of  $H_0$  to that determined assuming the cluster gas to be isothermal at the central temperature. The ASCA constraints on the thermal structure (see Fig. 3) limit  $H_0/(H_0)_{iso} = 1.13 \pm .02$

at 68% confidence.

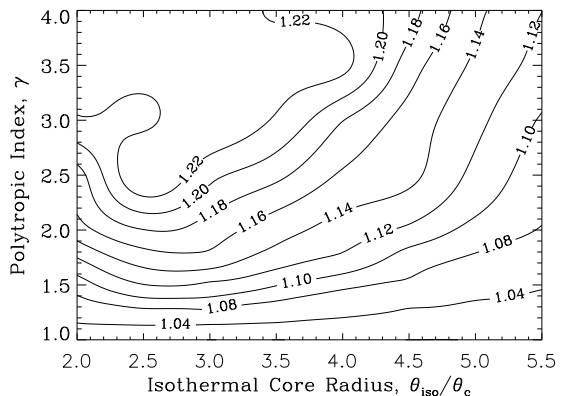


Fig. 7.— Ratio of the true Hubble constant to the isothermal value ( $H_0/(H_0)_{iso}$ ) as a function of the hybrid thermal model parameters. The value of the central temperature is assumed to be constant.

We also calculate  $H_0$  as a function of thermal structure for the more realistic case in which only the emission-weighted average X-ray temperature is known. The values of the normalization factors ( $N_X$ ,  $N_{SZ}$ ) are nearly unchanged from the previous case. Assuming the ASCA thermal structure, the central temperature is about 7% higher than the emission weighted average value. This leads to a larger offset in  $H_0$  from the isothermal value than when the central temperature is held fixed. In Figure 8, we plot the ratio of the true Hubble constant to that calculated assuming the cluster gas to be isothermal at the emission-weighted average temperature. The ASCA constraints on the thermal structure (see Fig. 3) limit  $H_0/(H_0)_{iso} = 1.29^{+.10}_{-.10}$  at 68% confidence. Inagaki *et al.* (1995) have investigated the effect of thermal structure on the value of  $H_0$  determined from the S-Z effect. For a simulated ‘‘Coma-like’’ cluster, they

found  $H_0$  to be underestimated by  $> 20\%$  when the IC gas was assumed to be isothermal. They identify uncertainty in the temperature profile as the most serious systematic error in the value of  $H_0$  and as a possible source of the “low” values sometimes found with the S-Z effect.

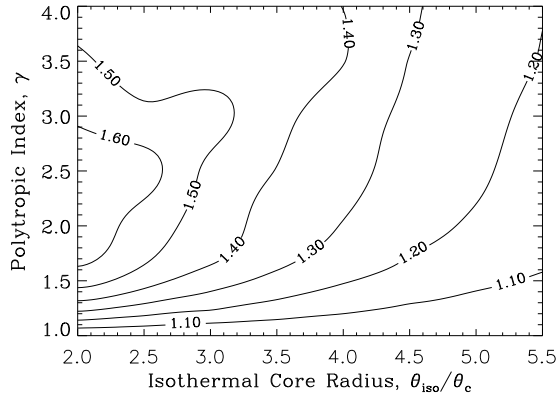


Fig. 8.— Ratio of the true Hubble constant to the isothermal value ( $H_0/(H_0)_{iso}$ ) as a function of the hybrid thermal model parameters. The value of the emission-weighted average temperature is assumed to be constant.

We have determined  $H_0$  under the assumption of the ASCA/GIS+SIS thermal structure modeled by the adopted hybrid model (Table 1). We find  $H_0(q_0 = \frac{1}{2}) = 78^{+54}_{-28} \text{ kms}^{-1} \text{ Mpc}^{-1}$  at 68% confidence, where we include uncertainties in the normalizations ( $N_X$  and  $N_{SZ}$ ) and density and temperature models. The uncertainties in the X-ray normalization and the density model are considered to be the same as in the isothermal case and all errors are added in quadrature. The individual contributions to the uncertainty in  $H_0$  are listed in Tables 3 and 6.

## 8. Additional Uncertainties

The uncertainties discussed so far are associated with the precision of the measurements required for the determination of the Hubble constant. We identify several additional sources of systematic uncertainty associated with assumptions we have made in order to determine  $H_0$  from the measured data. Among these are deviations from spherical symmetry, peculiar velocity, IC gas clumping, and astrophysical confusion. The contribution of each of these addi-

tional sources of uncertainty to  $y_0$  and  $H_0$  are listed in Tables 5 and 6 respectively.

### 8.1. Deviations From a Spherical Gas Distribution

The assumption that the extent of the IC gas along the line of sight is the same as is measured in the plane perpendicular to the line of sight is fundamental to this method for determining  $H_0$ . If the distribution of the IC gas is prolate (oblate) with its dimension along the line of sight longer (shorter) by a factor  $Z$  than the average of the dimensions perpendicular to the line of sight, then the derived  $H_0$  will be modified from the true  $H_0$  by a factor  $1/Z$  (BHA). The average Hubble constant derived from measurements of  $N$  clusters,  $\bar{H}_0 \propto \frac{1}{N} \sum_{n=1}^N \frac{1}{Z_n}$ , will be weakly biased towards higher  $H_0$  depending on the distribution of ellipticities contained in the sample. In this paper, we quantify the contribution of asphericity to the uncertainty in  $H_0$  determined from measurements of a single cluster. We estimate this contribution from the statistics of the ellipticity of the observed X-ray isophotes of a sample of other clusters.

McMillian *et al.* (1989) determined the ellipticity of the X-ray isophotes for a sample of 49 clusters. The average ellipticity for this sample is  $\bar{\epsilon} = .277$ . This average has been computed without the removal of any of the clusters containing obvious substructure. For a sample of clusters, the average elongation or shortening along the line of sight will be smaller than the average deviation from circularity of the projected X-ray isophotes. Departures from sphericity of the IC gas distribution, therefore, contribute an uncertainty of  $< \pm 27.7\%$  to the determination of  $H_0$  from a single cluster.

### 8.2. Peculiar Velocity

If the IC gas has a bulk velocity ( $\vec{v}_p$ ) with respect to the CMB rest frame, there is an additional kinematic component to the S-Z effect,

$$\Delta I_K = -I_0 \frac{x^4 e^x}{(e^x - 1)^2} \int n_e \sigma_T \frac{\vec{v}_p}{c} \cdot d\vec{l}. \quad (43)$$

In general, the ratio of the brightnesses of the kinematic and thermal components of the S-Z effect integrated over the 2.1 mm band is small. For A2163 ( $T_e = 12.4 \text{ keV}$ ),

$$\frac{\int \Delta I_K f(\nu) d\nu}{\int \Delta I_T f(\nu) d\nu} = .139 \left( \frac{v_r}{10^3 \text{ kms}^{-1}} \right), \quad (44)$$

where  $v_r = \vec{v}_p \cdot \vec{d}$  is the projection of the average cluster velocity onto the line of sight, and  $f(\nu)$  is the average transmission of the SuZIE system in the 2.1 mm band.

We have made additional measurements of A2163 with filter bands centered at 1.4 and 1.1 mm. Combining the mm-wavelength measurements with  $T_{e0}$  we are able to limit  $|v_r| < 1500 \text{ km s}^{-1}$  for A2163 (Holzapfel *et al.* 1996b). Bahcall *et al.* (1994) make theoretical predictions of the one-dimensional RMS cluster peculiar velocities for a variety of cosmological models. The results range from  $268 \text{ km s}^{-1}$  for  $\Omega = 0.3$  cold dark matter to  $614 \text{ km s}^{-1}$  for  $\Omega = 1.0$  hot dark matter. We expect the S-Z results to reach this level of accuracy soon; until they do, we adopt these theoretical limits to constrain the peculiar velocity. For the largest predicted peculiar velocities, we find  $\Delta y_0/y_0 = \pm 7.4\%$  and  $\Delta H_0/H_0 = {}^{+16.6}_{-13.3}\%$ .

### 8.3. Isobaric Inhomogeneities

Clumping of the IC gas on sufficiently short scales could escape detection with the ROSAT/PSPC. Hydrodynamical simulations of subclustering by Inagaki *et al.* (1995) indicate that clumping could result in an overestimation of  $H_0$  by as much as 10–20%. Here we consider to what extent the existence of such clumps could effect the measurement of  $H_0$  for A2163.

We assume a simple model for the clumping consisting of a two-phase medium in pressure equilibrium: a hot phase of temperature  $kT_h$ , and cooler clumps overdense by a factor  $B$  with respect to the hot phase. The clumps are assumed to be uniformly distributed in volume with filling factor  $f$ . In principle, such clumping can be constrained by X-ray spectral data; this is equivalent to placing limits on the superposition of two isothermal models with the same form for their average density profile and temperatures  $kT_h$  and  $kT_c = kT_h/B$ . We define a normalization factor  $N_C \propto n_{e0h}^2 kT_h^2$ , where  $n_{e0h}$  is the central electron density of the hot phase.  $N_C$  is normalized to the best fit value obtained with the isothermal model; in the presence of clumping,  $H_0/H_{0,iso} = N_C$ .

We fit the GINGA + ROSAT/PSPC spectral data with this model, leaving  $f$ ,  $B$ ,  $kT_h$ , and  $N_C$  free to vary. The hydrogen column density and the iron abundance are also left free to vary, but are constrained to have the same value for the two phases. The relative normalization between the PSPC and GINGA data is fixed to the best value obtained from

the isothermal model. The best fit is obtained for a nearly isothermal model:  $kT_h = 15.5 \text{ keV}$ ,  $B = 1.15$ , and  $N_C = 0.98$ , with no significant improvement in the fit as compared to the isothermal model. The 68% confidence contours for the two parameters  $kT_h$  and  $B$  are plotted in Fig. 9, with lines corresponding to equal  $f$  values superimposed. In Fig. 10 we have plot the 68% confidence contours for the two parameters  $kT_h$  and  $N_C$ ; it is apparent that the data prohibit low values of  $N_C$ .

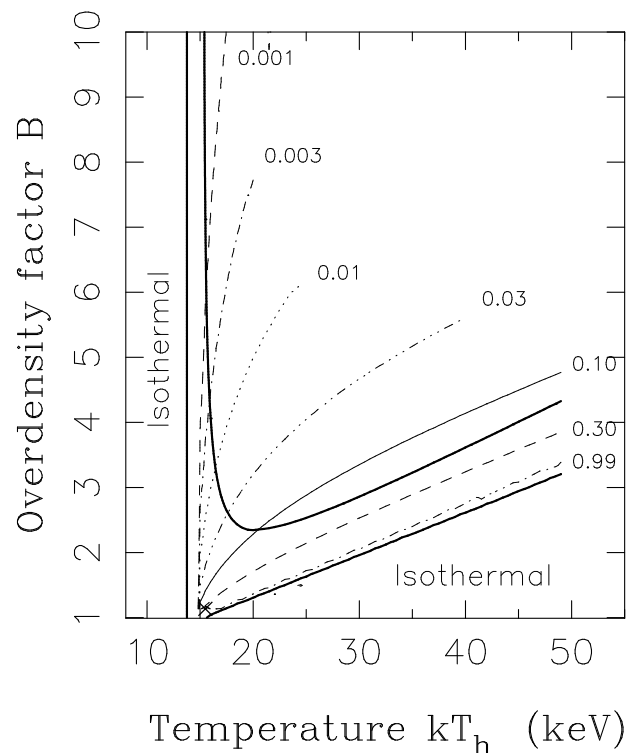


Fig. 9.— Contour map for the two parameters  $kT_h$  and  $B$  of the isobaric clumping model.  $kT_h$  is the temperature of the hot phase and  $B$  is the overdensity factor of the clumps. The heavy line represents the limits at 68% confidence, and is determined by fitting the GINGA + ROSAT/PSPC spectral data. Contours of equal filling factor  $f$  are indicated by the broken lines. The best fit point is indicated by a cross.

In the extreme case of large  $kT_h$  values, the gas must contain clumps at temperature  $\sim kT_{iso}$  embedded in a significantly hotter phase. In the GINGA energy band, the emissivity is a weak function of the temperature for  $kT \geq 20 \text{ keV}$ ; therefore, it is difficult to constrain high values for  $kT_h$ . However, large val-

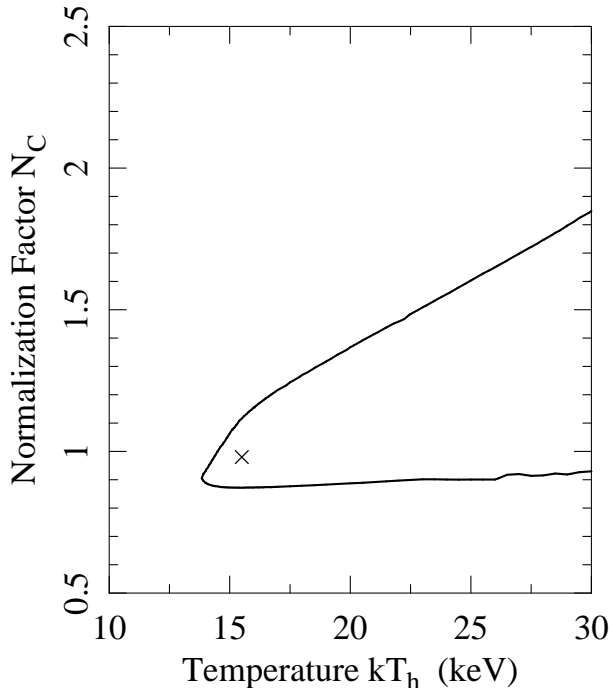


Fig. 10.— Contour map for the two parameters  $kT_h$  and  $N_C$ . The normalization factor,  $N_C$ , is defined such as  $N_C = H_0/H_{0,iso}$ . A heavy line marks the limits at 68% confidence. The best fit point is indicated by a cross.

ues of  $kT_h$  are unlikely. Unless electron thermal conduction is strongly suppressed by IC magnetic fields, the clumps would evaporate on a time-scale much shorter than the Hubble time. The evaporation of clumps in a hot phase has been studied by Cowie & McKee (1977) and Balbus & McKee (1982). When the scale of the thermal structure is less than the electron mean free path, the evaporation is governed by the saturation parameter,  $\sigma_0$ . At a redshift of  $z = .2$  and  $H_0 = 50 \text{ kms}^{-1} \text{ Mpc}^{-1}$  one half of the ROSAT/PSPC PSF FWHM is 50 kpc. For clump radii smaller than this scale and density less than  $6 \times 10^{-3} \text{ cm}^{-3}$ , the conduction is saturated ( $\sigma_0 > 1$ ). The evaporation time is then given by

$$t_{evap} = 1.0 \times 10^7 B \left( \frac{kT_h}{15 \text{ keV}} \right)^{-1/2} \left( \frac{R_c}{50 \text{ kpc}} \right) \sigma_0^{-0.209} \text{ yr}, \quad (45)$$

which is always much shorter than the Hubble time.

Considering only the effect of clumps colder than the bulk of the IC gas, we determine  $\Delta H_0/H_{0,iso} =$

$-10.0\%$  at 68% confidence. We have not treated the case in which the modeled IC gas also exhibits large scale thermal structure; we expect the restrictions on the presence of cool clumps to be even tighter in this case. It must be pointed out that these limits apply only to IC gas which is static and free of strong magnetic fields, IC gas that does not satisfy these conditions could be considerably more clumped.

#### 8.4. Astrophysical Confusion

Although astrophysical confusion from randomly distributed sources is expected to be small at millimeter wavelengths (Fischer & Lange 1993), the possibility of confusion contributing a considerable systematic error to the determination of  $y_0$  must be considered. In this region of the sky, the amplitude of anisotropic interstellar dust emission calculated from the IRAS  $100 \mu\text{m}$  map and scaled with the sky-average spectrum of dust emission (Wright *et al.* 1991) is negligible. A VLA search towards A2163 shows evidence of a radio source  $0.8'$  west of the cluster center with an inverted spectrum (Herbig & Birkinshaw 1992). For this source, the flux rises from 1 to 3 mJy between 6 and 2 cm, suggesting a flux as large as 30 mJy at 2.1 mm. However, Fischer & Radford report an upper limit of 5 mJy ( $2\sigma$  in a  $20'' \delta$ ,  $10''$  RA beam) on point source emission within  $1'$  of the X-ray center at a wavelength of 3.3 mm. For the adopted hybrid model, a 5 mJy point source at 2.1 mm would cause the underestimation of the peak Comptonization by  $\Delta y_0 = +0.24 \times 10^{-4}$ . The sign reflects the fact that the only known radio source in the scan with a flux and spectrum such that it could contribute significantly is sufficiently close to the S-Z center that it would decrease the size of the measured S-Z decrement. A2163 exhibits the brightest radio halo yet discovered (Herbig & Birkinshaw 1995). From measurements at 1.5 and 4.9 GHz, the integrated flux from the radio halo is estimated to be less than 1 mJy in the SuZIE 2.1 mm band (Herbig 1995). This could contribute at most  $\Delta y_0 = \pm 0.05 \times 10^{-4}$  to the peak Comptonization. We can use these results to place a conservative limit on the contribution of radio confusion to the uncertainty in the peak Comptonization,  $\Delta y_0 = {}^{+0.25}_{-0.05} \times 10^{-4}$ .

It is also possible for the measurement of the S-Z effect to be confused by the presence of primary CMB anisotropies. Haehnelt and Tegmark (1996) estimated the confusion limits from primary anisotropies to the determination of cluster peculiar velocities. We

use their results to determine the effect of primary anisotropies on the measurement of the peak Comptonization. For  $\Omega = 1$  (CDM) models with  $\Omega_{baryon} = .01 - .1$ , cluster optical depth  $\tau = 0.015$ , and the SuZIE beam size, they find  $|\Delta v_{pec}| < 300 \text{ kms}^{-1}$ . From this, we determine that primary anisotropies contribute an uncertainty of  $\Delta y_0/y_0 = \pm 3.6\%$  to the peak Comptonization parameter in A2163.

## 9. Conclusion

We have confirmed the previous detection of the S-Z effect in A2163 at 2.1 mm (Wilbanks *et al.* 1994). The 1993 and 1994 data sets have been analyzed using a relativistically correct treatment for the S-Z effect and the ROSAT derived density profile. Assuming an isothermal IC gas at the estimated GINGA+ASCA isothermal temperature,  $T_e = 12.4_{-1.9}^{+2.8} \text{ keV}$ , and including uncertainties in the fit amplitude, baseline, calibration, position, and density model, we find  $y_0 = 3.73_{-.61}^{+.48} \times 10^{-4}$ . Combining the S-Z and X-ray data and including uncertainties due to the S-Z and X-ray normalizations and isothermal IC gas temperature, we find  $H_0(q_0 = \frac{1}{2}) = 60_{-23}^{+41} \text{ kms}^{-1} \text{ Mpc}^{-1}$ .

There are indications that the IC gas in A2163 is not isothermal. Recent ASCA results suggest a dramatic decrease in the temperature of the IC gas with radius (Markevitch *et al.* 1996). The model used by Hughes *et al.* (1988) to fit the thermal structure in the Coma cluster is generalized and used as a two parameter fit to the temperature profile in A2163. We use the combined analysis of the S-Z and X-ray surface brightnesses to place limits on models for the thermal structure of the gas. This is the first application of, what is potentially, a powerful probe of the state of the IC gas. So far, the S-Z measurements lack sufficient sensitivity to distinguish between the thermal structure indicated by the ASCA results and an isothermal IC gas.

Adopting the ASCA thermal structure, a joint analysis of the GINGA and ASCA/SIS+GIS thermal structure yields a central temperature,  $T_{e0} = 13.3_{-1.7}^{+2.8} \text{ keV}$ . Using this thermal structure, and including uncertainties due to the baseline, calibration, and density and temperature models, we determine  $y_0 = 3.07_{-.54}^{+.40} \times 10^{-4}$ . Combining the X-ray and S-Z results and including uncertainties due to the S-Z and X-ray normalizations and central temperature, we find  $H_0(q_0 = \frac{1}{2}) = 78_{-28}^{+54} \text{ kms}^{-1} \text{ Mpc}^{-1}$ .

There are several additional contributions to the

uncertainties in  $y_0$  and  $H_0$ . It is possible that the cluster gas distribution is aspherical. We use the X-ray morphologies of a sample of clusters to estimate this contribution to the uncertainty in  $H_0$  determined from a single cluster. If the cluster exhibits a significant peculiar velocity there is an additional kinematic component to the S-Z effect. We use theoretical estimates of cluster peculiar velocities to constrain the contribution of the kinematic effect to the uncertainty in  $y_0$  and  $H_0$ . An IC gas that contains clumps could bias the value of  $H_0$ . The ROSAT/PSPC + GINGA spectrum is used to constrain the contribution that clumped IC gas could make to the value of  $H_0$ . Finally, it is possible that the S-Z effect is astrophysically confused. We use theoretical and observational results to limit the uncertainty associated with astrophysical confusion, including primordial anisotropies of the CMB. The contributions to the uncertainty in  $y_0$  and  $H_0$  due to each of these sources are listed in Tables 5 and 6. Including these additional sources of uncertainty in the analysis which adopts the ASCA thermal structure, we determine  $y_0 = 3.07_{-.60}^{+.54} \times 10^{-4}$  and  $H_0(q_0 = \frac{1}{2}) = 78_{-40}^{+59} \text{ kms}^{-1} \text{ Mpc}^{-1}$ .

There is an important distinction to be made between the uncertainties listed in Table 6, those that are essentially statistical and those that have a significant systematic component. Because we have no information about the extent of the IC gas along the line of sight, the IC gas is assumed to be spherically symmetric. We must average over a sample of clusters to reduce the contribution to the uncertainty due to asphericity of the IC gas. The uncertainties due to cluster peculiar velocities and primary CMB anisotropies are purely statistical and smaller than that due to cluster asphericity. These uncertainties, like the statistical uncertainties in the measured data, will be reduced for  $H_0$  determined from a sample of clusters.

A more serious obstacle to the determination of  $H_0$  is the presence of systematic errors which can contribute to the results for each of the members of a sample of clusters. If the IC gas has the thermal structure indicated by the ASCA results for A2163, assuming the gas to be isothermal results in the underestimation of  $H_0$  by  $\sim 30\%$ . To eliminate this source of uncertainty, the thermal structure of each cluster in the sample will have to be determined. All IC gas will be clumped to some degree; this biases the results for  $H_0$  to higher values. The presence of clumps could be better constrained by high resolution observations of the X-ray surface brightness, and improved

X-ray spectra. Astrophysical confusion of the S-Z effect by compact cluster radio sources can be virtually eliminated by observations with mm-wavelength interferometers. Uncertainty in the mm-wavelength flux of the planetary calibrators contributes  $\sim \pm 10\%$  uncertainty to the determination of  $H_0$ . The COBRAS/SAMBA satellite mission may be capable of relating planetary (and some S-Z) fluxes directly to the dipole anisotropy, which is known to a precision of  $\pm 0.2\%$  (Fixsen *et al.* 1996).

To determine an accurate value of  $H_0$  using the S-Z effect, we must reduce the potential sources of systematic error to below the level of the statistical uncertainties when averaged over a reasonable sample of clusters. Spatially resolved X-ray spectra obtained by the next generation of X-ray satellites will be essential to achieve this goal. Using the S-Z effect, it should then be possible to determine  $H_0$  to an accuracy of  $\lesssim 10\%$  with a sample of  $\sim 25$  clusters.

We would like to thank Maxim Markevitch and Koujun Yamashita for informative discussions concerning the ASCA results. The referee, Mark Birkinshaw, contributed several helpful comments which greatly improved the presentation of the results. Thanks to Antony Schinkel and the entire staff of the CSO for their excellent support during the observations. The CSO is operated by the California Institute of Technology under funding from the National Science Foundation, contract #AST-93-13929. This work has been made possible by a grant from the David and Lucille Packard foundation and by National Science Foundation grant #AST-95-03226.

## A. Appendix: Residual Common-mode Signal

In this appendix, we discuss the removal of the residual common-mode signal which is not removed in hardware due to the mismatch in the responsivities of the detectors in a difference. A mismatch in responsivities of  $\sim 1\%$  can contribute significant low frequency noise to a detector difference. Changes in the background loading of the detectors over the course of an evening can lead to responsivity mismatches of this size. Removing the residual common-mode signal typically reduces the noise determined from the distribution of scan amplitudes by  $\sim 10 - 20\%$  with no significant effect on the fit amplitudes.

For each difference, we determine the average common-mode correlation coefficients ( $\bar{\alpha}_k$ ) by aver-

aging  $\alpha_{kj}$  over the scans in a given period of observation; they are typically of order unity. Because of the difference in electronic gains between the single and differential signals, the amplitude of the source in the average single detector signal is smaller than in the differential signal by a factor  $G_s/G_d = 1/120$ . If  $s_{ji}$  and  $d_{kji}$  were completely correlated we would remove  $\bar{\alpha}(G_s/G_d) \sim 1\%$  of the differential signal.

In a drift scan across a stationary source, the difference of the signals from two perfectly matched detectors is orthogonal to their sum. The same is true for the signals ( $d_{31}$ ,  $t_{123}$ ,  $d_{64}$ , and  $t_{456}$ ) when compared to the average of all six single detector signals. The fraction of average single detector signal to which the differences are sensitive is proportional to the fractional mismatch of the detector differences, which is  $\sim \bar{\alpha}(G_s/G_d)$ . We estimate the amount of signal removed from the differential signals as the product of the size of the subtracted signal and its coupling to the detector differences to be  $\Delta y/y \approx [\bar{\alpha}(G_s/G_d)]^2 \sim 10^{-4}$ . Subtraction of the residual common-mode signal has a negligible effect on the determination of the source amplitudes.

## REFERENCES

- Alsop, D. C., Inman, C., Lange, A. E., & Wilbanks, T. 1992, *Applied Optics*, 31, 6610
- Arnaud, M., Hughes, J. P., Forman, W., & Jones, C. 1992, *ApJ*, 390, 345
- Avni, Y. 1976, *ApJ*, 210, 642
- Balbus, S. & McKee, C. 1982, *ApJ*, 252, 529
- Bahcall, N. A., Gramman & M., Cen, R. 1994, *ApJ*, 436, 23
- Birkinshaw, M. & Hughes, J. P. 1994, *ApJ*, 420, 33
- Birkinshaw, M., Hughes, J. P., & Arnaud, K. A. 1991, *ApJ*, 379, 466
- Cavaliere, A., Danese, L. & DeZotti, G. 1979, *A&A*, 75, 322
- Cavaliere, A. & Fusco-Femiano, R. 1976, *A&A*, 49, 137
- Chandrasekhar, S. 1950 *Radiative Transfer*, p. 17 (New York: Dover)

- Church, S. E., Ganga, K. M., Holzzapfel, W. L., Ade, P. A. R., Mauskopf, P. D., Wilbanks, T. M. & Lange A. E. 1997, ApJ, in press
- Cowie, L. & McKee, C. 1977, ApJ, 211, 135
- Elbaz, D., Arnaud, M., & Bohringer, H. 1995, A&A, 293, 337
- Fischer, M. L. & Lange, A. E. 1993, ApJ, 419, 194
- Fischer, M. L. & Radford, S. J. E. 1993, private communication
- Fixsen, D. J. *et al.* 1996, preprint
- Glezer, E. N., Lange, A. E., & Wilbanks, T. M. 1992, Applied Optics, 31, 7214
- Griffin, M. J., & Orton, G. S. 1993, Icarus, 105, 537
- Gunn, J. E. 1978, in Observational Cosmology, ed. A Maeder, L. Martinet & G. Tammann (Sauverny: Geneva Observatory), 1
- Haehnelt, M. G. & Tegmark, M. 1996, MNRAS, 279, 545
- Herbig, T. & Birkinshaw, M. 1992, private communication
- Herbig, T., Lawrence, C. R., Readhead, A. C. S., & Gulkis, S. 1995, ApJ, 449, L5
- Herbig, T. & Birkinshaw, M. 1995, BAAS, 26, 1403
- Herbig, T., private communication 1995
- Holzzapfel, W. L., Wilbanks, T. M., Ade, P. A. R., Church, S. E., Fischer, M. L., Mauskopf, P. D., Osgood, D. E., & Lange, A. E. 1997, ApJ, in press
- Holzzapfel, W. L., Ade, P. A. R., Church, S. E., Mauskopf, P. D., Rephaeli, Y., Wilbanks, T. M. & Lange, A. E. 1997, ApJ, in press
- Hughes, J. P., Gorenstein, P., & Fabricant, D. 1988, ApJ, 329, 82
- Hughes, J. P., Butcher, J. A., Stewart, G. C., & Tanaka, Y. 1993, ApJ, 404, 611
- Inagaki, Y., Sugimotohara, T., & Suto, Y. 1995, PASJ, 47, 411
- Jones, M. *et al.* 1993, Nature, 365, 320
- Kompaneets, A. S. 1957, Soviet Physics-JETP, 4, 730.
- Markevitch, M., Mushotzky, R., Inoue, H., Yamashita, K., Furuzawa, A., & Tawara, Y. 1996, ApJ, 456, 437
- Mather, J. C. *et al.* 1994, ApJ, 420, 439
- McMillian, S. L. W., Kowalski, M. P., & Ulmer, M. P. 1989, ApJS, 70, 723
- Myers, S. T., Baker, J. E., Readhead, A. C. S., & Herbig, T. 1995, preprint
- Rephaeli, Y. & Lahav O. 1991, ApJ, 372, 21
- Rephaeli, Y. 1995a, ARA&A, 33, 541
- Rephaeli, Y. 1995b, ApJ, 445, 33
- Soucail G., Arnaud M., & Mathez G. 1996, in preparation
- Squires, G., Neumann, D. M., Kaiser, N., Arnaud, M., Babul, A., Bohringer, H., Fahlman, G., & Woods, D. 1997, ApJ, submitted
- Sunyaev, R. A. & Zel'dovich, Ya. B. 1972, Comments on Astrophysics and Space Physics, 4, 173
- Sunyaev, R. A. & Zel'dovich, Ya. B. 1980, MNRAS, 190, 413.
- Wilbanks, T. M., Ade, P. A. R., Fischer, M. L., Holzzapfel, W. L., & Lange, A. E. 1994, ApJ, 427, L75
- Wright, E.L. 1979, ApJ, 232, 348
- Wright E.L. *et al.* 1991, ApJ, 381, 200
- Zel'dovich, Ya. B. & Sunyaev, R. A. 1968, Ap&SS, 4, 301